# Ambient Seismic Noise Tomography and Structure of Eastern North America

Chuntao Liang (cliang1@memphis.edu), Charles A. Langston (clangstn@memphis.edu)

Center for Earthquake Research and Information, The University of Memphis

Memphis, TN, 38152, USA

Submitted to JGR

(October 2007. Revised)

**Abstract:** The time derivative of cross-correlation functions (CCF) of ambient noise fields recorded by two stations can be approximated as the Green's Function (GF) between the stations. The CCFs are thus used as Peudo-GFs (dominated by surface waves) to invert for group velocity structure in eastern North America. Stations from two regional networks deployed to monitor the New Madrid Seismic Zone and eastern Tennessee seismic zone, together with stations of the US National Seismic Network, greatly improve tomographic ray coverage. The short period (T=5 seconds) group velocity map shows strong correlations with the depth to Precambrian basement. Many subtle local structures can be clearly identified from the velocity map, including the Ozark uplift, Cincinnati Arch, Nashville Dome and the Blue Ridge province of the Appalachians showing relatively high group velocity. The long period (T=15 seconds) group velocity map shows strong correlations with regional geology. Ancient rift basins, such as the Mid-Continent Rift (MCR) system, the Reelfoot rift, the Oklahoma Aulacogen and the Eastern Continent Rift, are associated with low velocity belts along their rift axes. We also find that all major seismic zones in eastern North America, such as the New Madrid seismic zone, Eastern Tennessee seismic zone as well as Ouachita Orogen seismic zone, are approximately located at transition zones separating velocity highs and lows. This observation suggests that those seismic zones may reflect the reactivation of ancient faults associated with continental rift and collision zones.

# 1. Introduction.

## 1.1 Geological and geophysical background for eastern North America (ENA).

The North American continent east of the Rocky Mountains is not particularly tectonically active today but records several Wilson cycles in its structural and geological framework (*Hatcher* 1989). Although the overall history of the continent is known in broad overview, there remain important gaps in knowledge concerning the location and nature of ancient plate boundaries and the relationship of lithospheric heterogeneity to present day seismic zones. The central and eastern U.S. is located well away from the current plate boundaries of the North American plate yet contains one of the more fascinating scientific problems of major intraplate seismicity that is seemingly inconsistent with the tenets of plate tectonics.

The primary example is the New Madrid Seismic Zone (NMSZ, Figure 1b). Continuing high rates of small magnitude earthquakes, the great historical earthquakes of 1811-1812 and large paleoseismic earthquakes define the NMSZ as one of the major intraplate seismic zones of the world [*Johnston & Schweig*, 1996]. The tectonic mechanism of intraplate seismicity, however, remains a major unresolved problem in modern geology. The Paleozoic framework of the region is dominated by a passive margin that evolved into a convergent margin during the Appalachian-Ouchita orogeny. These orogenic belts are recognized as being among the major continent-continent collision belts of the world and many geological concepts originated from the study of this mountain chain [*Hatcher* 1989]. This orogenic belt separates the North America Craton from the Atlantic coastal plain to the east and the Gulf coastal plain to the south. Coexisting with convergent boundaries in ENA are divergent belts, such as the Mid

Continental Rift system (MCR, Figure 1a & 1b) [*Hinze et al*., 1997], the Reelfoot rift [*Ervin & McGinnis*,1975] and the postulated East Continental Rift Complex (ECRC) [*Stark*, 1997]. Since the majority of these ancient rifts as well as much of the Ouachita Orogen are buried under thick sediments, geophysical data are indispensable to obtain a better understanding of the tectonic evolution of ENA.

Extensive geophysical investigations have been conducted in ENA with many of the results being summarized by *Pakiser & Mooney*, [1989]. High resolution gravity (Figure 1b) and aero-magnetic datasets are reviewed in detail by *Kane & Godson* [1989], *Jachens et al.* [1989] and *Van der Voo* [1989]. A number of seismic reflection and refraction experiments have also been conducted, but they were designed to investigate local structure associated with the NMSZ, MCR and Appalachian and Ouachita orogenic belts [*Mooney et al*. 1983; *Catchings* 1999; *Phinney & Roy-Chowdhury* 1989]. Notably, extensive reflection profiles were collocated by the Consortium for Continental Reflection Profiling (COCORP) [*Phinney & Roy-Chowdhury* 1989]. However, these datasets are sparse at regional scales. There have been numerous efforts to use the seismic waves from NMSZ earthquakes and other diffusive seismicity in ENA to investigate the subsurface structure [*Herrmann*, 1973; *Herrmann & Fischer,* 1978; *Langston* 1994; *Langston et al.* 2003; *Vlahovic et al*., 2000; *Vlahovic* & *Powell*, 2001]. Due to the absence and uneven distribution of large earthquakes, and limited station distribution, however, these studies are limited to relatively shallow depths and small areas. *Van der Lee & Nolet,* [1997], *Godey et al*. [2003] and *Gaherty* [2004] used surface waves to investigate seismic structure on a lithospheric scale, but once again, due to the absence of dense ray coverage within the ENA, short wave length structures (from few tens of kilometers to 200 kilometers) are not resolvable.

All of above seismic studies, based on either passive or active seismic sources, yielded the structure in small regions with high resolution or over large regions with limited resolution. A large scale picture of seismic velocity structure with resolution from a few tens of kilometers to 200 kilometers has not yet been determined. In this study, we use the new noise data tomography technique to image the subsurface of ENA. Ambient noise data recorded by broadband seismometers are cross-correlated to extract Pseudo-Green's Functions (PGF). Traditional surface wave tomography methods are then used to process PGFs to produce maps of seismic structure in terms of group velocity at different periods. By this method, we will be able to image ENA with resolutions as high as 1°x1° for a period of 5 seconds and 2°x2° for a period of 15 seconds. Our results will show very strong consistency with other available geophysical datasets.

## 1.2 Theoretical background

As early as 1968, *Claerbout* [1968] pointed out that the reflectivity between two stations can be found by cross-correlating the transmission fields at the same two stations. In 1993, the cross-correlation of ambient noise fields on the Sun's surface inferred from Doppler Interferometry was successfully used to produce acoustic distance-traveltime curves of the Sun [*Duval et al*, 1993]. Soon after, robust observations were reported in many fields to show the similarity between the Green's function (GF) and the cross-correlation function (CCF) of ambient noise fields at two points. These include, for example, ultrasonics [*Weaver & Lobkis*, 2001, *Derode et. al*, 2003], underwater acoustics

[*Roux & Kuperman*, 2004], helioseismology [*Rickett & Claerbout*, 1999] and seismology [*Campillo & Paul*, 2003, *Shapiro & Campillo*, 2004, *Sabra et. al*, 2005a, *Yao et. al*, 2006, *Yang et. al*, 2007, *Villasensor et. al*, 2007, *Moschetti et. al*, 2007 and many others]. A number of theories have been proposed to explain the link between the Green's Function (GF) and Cross-Correlation Function (CCF) [*Claerbout*, 1968, *Lobkis & Weaver*, 2001, *Derode et al*, 2003, *Snieder* 2004, *Wapenaar*, 2004, *Roux et al*, 2005]. Most theories are based on the assumptions of an ideally random medium or evenly distributed sources. Other derivations are only valid in estimating certain types of GFs, for example, using cross-correlation of transmission fields to estimate the reflection responses [*Claerbout*, 1968, *Wapenaar*, 2004]. Extracted GFs are often dominated by surface waves and *Shapiro et al* [2005], *Sabra et al* [2005b] and many papers mentioned above were able to determine the surface wave group velocity. *Yao et al* [2006] were able to invert for surface wave phase velocity. *Bensen et. al* [2007] summarized the major steps to extract group and phase velocity and surface wave tomography. In this study, we basically apply the same steps as *Bensen et. al* [2007] to invert the extracted surface waves for group velocity.

## 2. Extracting Surface Waves from Ambient Noise and Group Velocity Tomography.

### 2.1 Extraction of Surface Waves

*Wapenaar* [2004] provided a rigorous derivation based on reciprocity theory to show the relationship between the Green's function (GF) and the cross-correlation function (CCF). Considering only the cross-correlation of vertical components of two stations at $\vec{x}_A$ and $\vec{x}_B$, in the frequency domain, equation (9) in *Wapenaar* [2004] can be simplified to:

$$C_{AB}^{3D}(\omega) = -\{G_{AB}(\omega) + G_{BA}^{*}(\omega)\}S(\omega) \qquad (1)$$

with $C_{AB}^{3D}(\omega) = \langle u_A \oplus u_B \rangle$. $u_A$ and $u_B$ are vertical wavefields at location $\vec{x}_A$ and $\vec{x}_B$, respectively. $C_{AB}^{3D}(\omega)$ gives the ensemble average of the cross-correlation of two wavefields over all noise sources in 3D space. $G_{AB}$ and $G_{BA}$ are the GFs corresponding to the responses at location $\vec{x}_A$ due to an impulse source at location $\vec{x}_B$ and the reverse direction, respectively. $S(\omega)$ denotes the spatial ensemble average of the power spectrum of the noise sources. *Snieder* [2004] used stationary phase approximation to evaluate the spatial ensemble average of $C_{AB}^{3D}(\omega)$ which should be integrated through 3D space. He found that if one multiplies the right hand side of equation (1) by $\frac{1}{i\omega}$, the integration can be reduced to the integration along the great circle path linking two receivers. That is, only the sources located along the receiver line are counted. This results in:

$$C_{AB}(\omega) = -\frac{1}{i\omega}\{G_{AB}(\omega) + G_{BA}^{*}(\omega)\}S(\omega) \qquad (2)$$

In the time domain, this equation states that: The time derivative of the CCF of two wavefields is proportional to the Green's functions between the two stations weighted by the ensemble average of the power spectrum of the noise sources, where the ensemble average is taken along the great circle path between the two receivers. *Lobkis & Weaver* [2001] and *Roux et al* [2005] arrived at a similar conclusion.

Equation (2) also shows that exact GFs can be extracted only when the ensemble average of the source power spectrum $S(\omega)$ is a constant. That is, in the time domain, the autocorrelation of the accumulated source function $s(t)$ is a delta function:

$$S(t) = s(t) \oplus s(t) = C\delta(t) \qquad (3)$$

Equation (3) however is often not true. We therefore prefer to call the time derivative of the CCF a pseudo-GF (PGF). To achieve a better approximation to equation (3), the following data processing criteria may be applied: (i) Use noise data with time durations as long as possible. Increasing the length of the noise recording is equivalent to catching more waves propagating between the two stations. After averaging, $S(t)$ will be closer to a delta function. *Sabra et al* [2005a] showed that the signal-to-noise ratio of the PGF is proportional to the square root of recording time; (ii) Avoid large earthquakes. The source spectrums of real earthquakes are often not impulsive due to complicated slip history and fault geometry and earthquake spectrums often dominate the CCFs , (iii) Apply narrow band pass filters to the raw data, because, in a relatively narrower passband, the approximation of constant “source” amplitude may be better.

Following these basic rules, we apply this technique to the ambient noise data recorded on seismic stations located in eastern Northern America (Figure 1). In this study, 10 hour or longer time series of pure noise are used for each correlation. After removing instrument responses, the noise time series are filtered in the period band 2.5-7.5 seconds, and 10.0-20.0 seconds with the central period for the two bands 5 and 15 seconds, respectively. The filtered waveforms are converted to 1-bit amplitude time series before cross-correlation [*Larose et al*, 2004]. We have analyzed vertical component ambient noise recorded by four major seismic networks (Figure 1) in March, April and June 2006. These stations include local seismic networks at the NMSZ and ETSZ with 11 and 10 seismometers, respectively, monitored by the Center for Earthquake Research and Information, University of Memphis, a regional seismic network with 10 broadband seismometers (monitored by St. Louis University), and 24 broadband seismometers of the US National Seismic Network. In addition to the basic rules for data processing, we applied another two rules for path selection. First we reduce the data redundancy. Since we have 11 stations closely deployed in the NMSZ (Figure 1), the paths from any other station to those stations are very close. We only pick the one with the strongest signal for inversion. Not doing so may result in the inversion being weighted towards those "repeated" paths. The same is done for the 10 stations in the ETSZ. About 717 paths are discarded in total. Second, to reduce the influence of correlations between two localized noise fields at two stations and also to avoid the strong effects of off-great circle propagation for short paths, we discarded paths with distances less than ~8 times of the wavelength. So for 5 and 15s waves, all paths with distances less than 100km and 400km are discarded, respectively. Fortunately, due to the nature of the station distribution, we have pretty good ray coverage in the central part of the study area where most of the short paths are located. So the reduction of short paths will not affect the results too much. As we show below, the horizontal ray coverage in central and eastern North America is greatly improved owing to the addition of data from the two local seismic networks. A resolution of 1 to 2 degrees can be achieved in this region.

As an example of the analysis, CCFs of station pair WVT-SLM are plotted in Figure 2a. Surface waves are dominant on the CCFs. It’s very interesting to find that surface waves are stronger on one side of the CCFs for a few days and then appear to be stronger on the opposite side for the next few days. We interpret this as being due to changes in directions of microseism propagation. The CCFs with no clear surface waves around the predicted time are discarded (light gray traces in Figure 2a) and the rest are stacked as shown in Figure 2b.

Figure 3 shows the stacked CCFs for the period band of 10-20 seconds arranged by distance between station pairs. Once again we find that surface waves dominate the CCFs and body waves are absent or within the noise level. Clear surface wave trains are observed for distances ranging from 20km to 2000km with an average group velocity of about 3.0 km/s. Similar results have also been obtained by many other authors using stations around the world, e. g., *Campillo & Paul* [2003] and *Sabra et al* [2005a] *Yang et. al* [2007], *Villasensor et. al* [2007], *Moschetti et. al* [2007] and many others.

Most CCFs have surface waves on only one side of zero lag, but other CCFs have surface waves on both sides, for example, WVT-SLM in Figure 2a, and DWPF-MPH and CBN-WVT in Figure 3. These CCFs appear to be asymmetrical. This may be due to the fact that the accumulated source functions are quite different in opposite directions. In this case, only the one with larger amplitude is analyzed in this study.

The relative strengths of PGFs are determined by the relative amount of propagating waves in different directions in the noise field. Thus, the amplitude of the PGFs are an indication of directionality of noise sources. Figure 2a shows the daily changes of noise directionality. In Figure 4, we arrange the CCFs for period band between 2.5s to 7.5s based on the azimuth of station pairs. These stations are located in the eastern Tennessee seismic zone (Figure 1). Surprisingly, for station pairs with azimuth less than 180º, the PGFs are only found on the positive side of the CCFs, contrary to those with azimuth larger than 180º. Same pattern is observed for period band between 10s to 20s. This striking azimuth feature implies that ambient noise sources are mostly located to the east of the seismic array. Together with the frequency characteristics of the CCFs and the geographic location of the seismic arrays, we conclude that background noise from the Atlantic Ocean dominates that from the Gulf of Mexico or the Pacific ocean. The Great Lakes may also contribute to the noise field as suggested by CCFs from stations located further north.

## 2.2 Group Velocity Dispersion

The standard FTAN (Frequency Time ANalysis) method [*Levshin et. al* 1992] is used to measure group velocity dispersion. For seismograms with lower signal-to-noise ratios (SNR), the technique involves “phase equalization” [*Levshin et al.* 1992] or “phase-matched filtering” [*Herrin & Goforth*, 1977] and is applied to increase the SNR. *Herrin & Goforth* [1977] provided the theoretical basis and working flow chart for this method. The implementation of this process is illustrated in Figure 5. In Figure 5a the blue line is the original seismogram (PGF of station AAM and ACSO, filtered between 10 to 20 seconds). The original seismogram is filtered using a series of Gaussian filters [*Hermann* 1973] with central periods ranging from 10 to 20 seconds with a 1 second interval. The envelope functions of the filtered seismograms, i.e. the FTAN spectrum, are plotted in Figure 5c with colors representing envelope amplitudes. The peaks (local and global) of envelope functions are shown as solid red triangles. Two strips of peaks (red colors in Figure 5c) are observed on this figure. By experience, the lower strip is identified as the fundamental mode Rayleigh wave. Group velocities along this strip are picked by hand with corresponding estimated error bars (vertical yellow bars). The error bar shows the range of 97.5% of the maximum amplitude associated with a peak. The length of this bar is treated as the group velocity error and will be used to weight the data in the tomographic inversion. These points define the initial measurement of the dispersion curve: group velocity $U(\omega)$ as a function of frequency $\omega$. The average phase $\psi(\omega)$ of the narrow-banded signal around frequency $\omega$ can be predicted to be $\psi(\omega)=\int_{\omega_0}^{\omega} r/U(\omega)d\omega$, with $r$ the distance and $\omega_0$ the minimum frequency (equal to $2\pi\frac{1}{10}$ in this case). Phase-equalization is done by shifting the phase of the Fourier spectrum of the original seismogram by $i\psi(\omega)$ for each $\omega$ and transforming back to the time domain. The new phase equalized time series is plotted in Figure 5b as a blue line. Compared to the original seismogram in Figure 5a (blue line), the SNR of surface wave is improved significantly. The new time series is then windowed using a cosine taper (red line in Figure 5b). The Fourier transform is applied to the windowed time series, the average phase added back in, then inverse transformed. This is plotted on Figure 5a as the red line. After this process, the background noise is effectively eliminated. Applying the FTAN method again to the new time series (red line in Figure 5a) yields Figure 5d. Compared to the original FTAN spectrum in Figure 5c, the new FTAN spectrum is much clearer, and the dispersion curve appears to be smoother. In particular, the error bars are relatively shorter than those in original FTAN spectrum. This method can also effectively separate multi-mode and multi-path waves.

### 2.3 Group Velocity Tomography

We adopt the method introduced by *Barmin et al*. [2001] to invert group dispersion to obtain a map of group velocity variation. The system of equations is given by:

$$\Delta t_{ij} = \sum_{k=1}^{N} d_{ijk} \Delta s_k \qquad (4)$$

or

$$\mathbf{d} = \mathbf{Gm} \; , \qquad (5)$$

where $\Delta t_{ij}$ is the travel time residual for the great circle path that links the $(i, j)th$ station pair; $d_{ijk}$ is the length of the $(i, j)th$ ray path in the $kth$ cell ($d_{ijk}$ is 0 if the $(i, j)th$ ray does not pass through the cell *k*); $s_k$ is the slowness (1/ group velocity) of the $kth$ cell. With this basic equation system, other routine techniques in tomography, such as data weighting, 2D Laplacian regularization, resolution and stability analyses are also applied. Implementations of these techniques are similar to *Liang et. al* [2004], but some new aspects for this study are described below. The final equation system is solved using a classic Least Square QR Decomposition (LSQR) method [*Paige and Sanders*, 1982].

A starting model consisting of the average group velocity for a certain period is needed to calculate the travel time residual terms in equation (4). After the FTAN analysis, we obtained 252 and 443 rays (Figure 6a) with good quality for T=5.0 and 15.0 seconds, respectively. Figure 6b shows group travel times plotted against distance for

T=5.0 and T=15.0. One straight line for each period is fitted using an interactive method [*Liang et. al* 2004]. The average group velocities are 2.9km/s and 3.1 km/s for T=5.0 and T=15.0, respectively. These values are consistent with the group velocity dispersion derived from earthquake surface waves in this region [*Mitchell & Herrmann* 1979]. Notice that the distance range of data points for T=5.0 extends from 100km to 1500km, but that for T=15.0 seconds is from 400km to 2000km. This is due to the attenuation of high frequency waves so that the corresponding PGFs are poorly extracted for station pairs with distances larger than 1500km. Only the region between 95°W and 75°W and 32°N and 44°N has good ray coverage for T=5s Rayleigh waves. So the tomography is only done within this region. On the other hand, lower frequency (long period) waves experience severe interference for short distances, and thus they are poorly present on the CCFs for distances less than 400km.

Two weighting schemes are applied to account for the uneven data distribution and data quality. The uneven data distribution is dealt with by balancing the relative values of the G matrix (equation 5) elements that reflect the total lengths of rays in each cell. Cells with large numbers are down-weighted. The details are described in *Liang et al.* [2004]. Data quality is determined by both the quality of PGFs and the errors of group time measurements using the FTAN method.

The quality of an extracted PGF varies with station pair owing to the uneven distribution and randomness of noise sources. We quantify the quality of PGFs by a number $q^{GF}$, with $0 < q^{GF} < 1$. This number is estimated by visual inspection. Higher SNR of PGFs are assigned with higher $q^{GF}$ values. As shown in Figure 5, the precision of group velocity measured by the FTAN method is determined by the length of the error bars. Calculated from the error bar width, $err^{Disp}$ , is assigned as the error of the dispersion curve. Finally, the quality of a PGF, $q^{GF}$ , and the error of the corresponding dispersion curve, $err^{Disp}$, are combined to give the quality factor $q^{Tim}$ of group times for each period and each path:

$$q^{Tim} = \frac{a * q^{GF}}{a + err^{Disp} / b} \tag{6}$$

where $a \geq 1$ and $b \geq 1$ are used to control the relative importance of $q^{GF}$ and $err^{Disp}$. Since $q^{GF} \leq 1$ then $q^{Tim} < 1$. When $err^{Disp}$ is very small, $q^{Tim}$ will be close to $q^{GF}$. In our final inversion, $a$ and $b$ values are assigned to be 10 and 2, respectively. The weighting of data quality is conducted by left-multiplying both sides of equation (5) by a weighting matrix $W$,

$$W\mathbf{d} = W\mathbf{Gm} \tag{7}$$

where $W$ is a diagonal matrix and the diagonal elements are the group time qualities $q^{Tim}$ for all data points. Then final equation system to be solved is then modified to:

$$\mathbf{d}' = \mathbf{G}'\mathbf{m} \tag{8}$$

with $\mathbf{d}' = W\mathbf{d}$ and $\mathbf{G}' = W\mathbf{G}$.

Consider two data points (group arrival times), for example, for different paths but the same period. PGFs for both paths may have the same high quality, say $q^{GF} = 1.0$, but errors $err^{Disp}$ in the dispersion for the two data points are 10 and 1 seconds, respectively. The quality factors $q^{Tim}$ for the two data points are then $0.67$ and $0.95$, respectively. These values are the diagonal elements of $W$ corresponding to these two data points. The first data point is down-weighted because of its large error in the dispersion measurement.

Traditional checkerboard tests are used to examine model resolution. The studied region is divided into regular cells with size $0.5° \times 0.5°$ and $1.0° \times 1.0°$ for T=5s and 15s, respectively. Synthetic data are generated using the actual station distribution, which are then inverted using the same inversion procedure and parameters as in the real data inversion. The checkerboard model is generated by perturbing the background model by ±0.3 km/s in velocity. The recovered models for T=5.0 seconds and a pattern size of $1.5° \times 1.5°$ is shown in Figure 7a. Figure 8a shows the checkerboard test for periods T=15.0 seconds and a pattern size of $3.0° \times 3.0°$.

We use the "resolvability" variable $\Re = \sum_{i=1}^{M} (v_i^t + v_i^r)^2 \Big/ 2\sum_{i}^{M} \left[(v_i^t)^2 + (v_i^r)^2\right]$ defined by *Zelt* [1998] to quantify the differences between the true model and the recovered model. Where $v_i^t$ and $v_i^r$ are the true and recovered velocity anomalies at cell *i* inside a given operating area of M cells. We choose an operating area of $3.0^o$x$3.0^o$ centered on the cell for which we want to calculate the resolvability. For the 0.5 degree cell spacing, M=36. $\Re$ is calculated for each cell. When the recovered velocity and the true velocity of one cell is identical, then $\Re = 1$. The $\Re$ value decreases as the difference between two models increases. Cells with resolvability above some threshold value $\Re_0$ are defined to be resolvable. In Fig. 7a and 8a, the white thick contours correspond to $\Re_0 = 0.7$. The regions enclosed by these curves are defined to be the resolvable regions for corresponding pattern sizes. Checkerboard tests with pattern size of $1.0^o$x$1.0^o$, $1.5^o$x$1.5^o$, $2.0^o$x$2.0^o$, $2.5^o$x$2.5^o$, $3.0^o$x$3.0^o$ were conducted and the resolvable regions for different pattern sizes are plotted in Figure 7b and 8b for T=5s and T=15s, respectively. Owing to the dense seismic networks in the NMSZ and ETSZ (Figure 1 and Figure 6a), our resolution in the central part can be as high as $1.0^o$x$1.0^o$ and $2.0^o$x$2.0^o$ for T=5s and for T=15s, respectively.

## 3. Group Velocity Variation in the Central and Eastern U.S.

We inverted group velocities for periods T=5.0s, 7.5s, 10s, 12.5s, 15s, 17.5s and 20s. In this paper we choose 5s and 15s velocity maps to discuss shallow and whole crust structure, respectively (Figure 9 and 10). Other periods will be published together with the 3D inversion separately. Rayleigh waves with period of 5 seconds sample approximately the top few kilometers of the crust while T=15 waves sample almost the whole crust. Since the sensitivity of Rayleigh waves to the medium decreases with depth, the group velocity at one point can be treated as weighted average of the vertical velocity column with weights decreasing with depth.

Figure 9 is the group velocity map for period T=5.0 seconds. Refer to the Figure 1 for locations of geological units. Low velocity appears to be correlated with regions with thick sediments, such as, in the eastern Illinois Basin, the western Appalachian foreland basin, the Black Warrior basin in central Alabama, the Mississippi embayment, the Atlantic coastal plain and the central part of the Appalachian Mountains at the Tennessee North Carolina border where sediment is as thick as 3 km. A low velocity anomaly is present along the trend of the Missouri Batholith. This low velocity belt extends from the NMSZ northwestward and approximately overlaps with the low isostatic gravity anomaly (Figure 1b) associated with the granitic Missouri batholith [*Hildenbrand and Hendricks*, 1995].

High velocity anomalies are observed to correlate with regions with thin sediments, especially in tectonically uplifted regions. These include, the Ozark Dome where the Precambrian basement outcrops with the St. Francois Mountains in southeastern Missouri, the Nashville dome in central Tennessee, the Cincinnati arch, and the Appalachian Mountains excluding the central part. A velocity contrast is present across the eastern border of the Mississippi Embayment (Figure 9).

The NMSZ is located in a low velocity zone and appears to be confined by surrounding high velocity bodies. Wabash valley seismicity is scattered in a region with higher than average velocity but surrounded by high velocity bodies to the west (Ozark uplift), north and southeast. The linear ETSZ is located in a transition zone where velocity is high to the east and low to the west.

Figure 10 is the group velocity map for period T=15.0 seconds. This map shows strong correlations with the regional geology. The most spectacular features are the prominent low velocity anomalies associated with the three arms of the inferred Triassic triple junction located at the border of Oklahoma and Texas [*Jachens et al*, 1989]. The eastern arm of the triple junction extends approximately along the collision belt of the Ouachita orogeny to meet the south tip of the Appalachian Mountains. Low velocity is also observed to connect to the Mid Continental Rift in the Lake Superior region and its southeastward extension to Michigan basin, although the resolution is low in this region. Low velocity is also present in the Reelfoot rift in the western Mississippi embayment. The Wisconsin Arch is expressed as a prominent low velocity and low gravity zone [*Collinson et al*, 1988]. Central Ohio and western Kentucky may be associated with the Appalachian basin. The Atlantic Coastal Plain is present as low velocity as well except for a prominent velocity high observed in southern Georgia.

Similar to the short period (T=5.0 seconds) group velocity map, the Appalachian Mountains are characterized by high velocities except for the central part. High velocity is present to the east of Mississippi Embayment and this velocity high extends eastward to join the southern Appalachian Mountains. One east-west striking linear velocity high is present in northeastern Louisiana and the southwestern Mississippi border. This structure has 10 km of sediment thickness as well as extremely high bouguer gravity [*Jachens*, 1989, *Bassin et al*, 2000]. Another prominent north-south striking high velocity belt is located to the east of the Mid Continental Rift and extends southward to the Ouachita Mountains. The anomaly appears to be associated with north-south striking upper Paleozoic sedimentary units. A strong localized high velocity anomaly is present in the southern Georgia and may be associated with an isolated intrusion [*Jachens et al.* 1989].

The NMSZ and Wabash seismic zone are located in a transition zone with velocity highs to the east and southeast and velocity lows to the west and northwest. The ETSZ is, however, located at the western border of a high velocity body. Also note a linear belt of seismicity extending east to west direction from the southern tip of the Appalachian Mountains to southern Oklahoma, informally named the “Ouachita Orogen Seismic Zone” in this study, is approximately located at a low-high velocity transition zone.

To test whether the striking linear low velocity belts in the long period group velocity map are due to the smearing of some localized low velocity bodies, we conduct a “spike” test as shown in figure 11. The synthetic model consists of a background model with a constant velocity 3.1km/s and some localized low velocity spikes with a velocity of 2.8km/s (doted grids on Figure 11). Figure 11 shows the inverted model based on the synthetic travel times. No obvious smearing is observed for major linear structures such as the Mid-Continental Rift and the north-south low velocity belt from southern Wisconsin to Arkansas. However, smearing is indeed present at the Michigan basin where the azimuth distribution of rays are poor (Figure 6a and Figure 11).

## 4. Discussion.

### 4.1 Low velocity belts and the ancient rift system.

Failed continent rift systems are generally characterized by deep sedimentary basins filled with low velocity and low density clastic rocks [*Kearey and Vine*, 2004]. In many cases when the extruded or intruded volcanic rocks are well preserved in the center of a rift basin, an extremely high Bouguer gravity anomaly flanked by background low gravity anomalies on both sides will be observed along the rift axis [*Allen et al*. 1992]. The Mid Continent Rift (MCR) is one of the best examples with such gravity characteristics [*Hinze et al*, 1997]. The MCR is thought to be a failed Proterozoic rift zone extending from Lake Superior southwestward into Kansas and southeastward into the Michigan Basin (Figure 1b). The Lake Superior region is the only segment along the MCR where volcanic rocks (Keweenawan group) are exposed [*Allen et al*. 1992 and *Hinze* et al 1997]. By examining well log data, gravity and magnetic data as well as reflection and refraction profiles in the Lake Superior region, they pointed out that the centered gravity highs are a result of high density volcanic rocks [*Allen et al*. 1992] while the much wider region of gravity lows can be accounted by a wide subsidence sedimentary basin combined with underplated lower crust as the remnant of the Keweenawan hotsopt. A number of similar studies along other portions of the MCR revealed similar features [*Berendsen et al.* 1988, *Anderson* 1990]. *Hinze et al* [1997] summarized previous studies conducted along the MCR and found that the sedimentary layers in the MCR are as thick as 5km to 10 km. Our surface wave data shows that low velocity sedimentary layers near the surface have strong influences on group velocity dispersion at short periods. Thus, the prominent linear low velocity belts present in our results may be used to trace the sedimentary valleys associated with the failed rift system or Aulachogen.

On our T=15 seconds group velocity map (Figure 10), prominent low velocity anomalies are present in the Great lakes region and extend further southeastward to the Michigan basin and stop at the Michigan-Ohio border. This LVB approximately follows the trace of gravity highs associated with the east limb of the MCR. Because of the shortage of ray coverage, the LVB associated with the west limb is only visible from southeastern Nebraska into eastern Kansas. However, this LVB extends further southward to intersect the Oklahoma Aulocogen. *Adams and Keller* [1993] studied the stratigraphy, the ages and lithologic properties of volcanic rocks and found strong similarities between those in western Oklahoma, Texas and eastern New Mexico with the identified MCR and suggested that the MCR may actually extend further southwest from its west limb terminus in Kansas. Their suggestions are also supported by *Yarger* [1985] and *Nixon* [1988]. Our results provide additional geophysical evidence to support their conjecture, that the west limb of the MCR extends all the way from the Lake Superior to at least western Oklahoma (and possibly further south to western Texas and eastern New Mexico) with the southern portion less developed than its northern counterpart.

It is interesting to find that a LVB starting at the Reelfoot rift extends further north to intersect the low velocity belt in Great Lakes area. At the northernmost end of this LVB located in Wisconsin, it is associated with a SW-NE striking belt with relatively low crust velocity, high magnetic gradient and large negative isostatic gravity (Figure 2) [*Braile et al*, 1989] called the Wisconsin Arch [*Collinson et al.* 1988; *Jachens et al.*, 1989]. The segment between the Reelfoot rift and the Wisconsin Arch is termed the

Mississippi River Arch [*Collinson et al.* 1988] which also corresponds to relatively low Bouguer gravity compared to a higher Bouguer gravity anomaly in eastern Illinois [Plate 1 of *Jachens et al.* 1989, also Figure 2 for isostatic gravity]. The whole north-south striking LVB is associated with lower or middle  Paleozoic sedimentary rocks at the surface, which are older than the Upper Paleozoic rocks to east and west  (Figure 1 and 10).

### 4.2 The Appalachian Mountains

The Appalachian Mountains were created at the passive continental margin of ancient North America as a result of closing of the Iapetus ocean and suturing of north America with Africa in mid- to late Paleozoic [*Hatcher* 1989]. Collision events created a series of distinct litho-tectonic provinces from west to east: the deep Appalachian foreland basin, the thrust and fold belts (Valley and Ridge province), uplifted Precambrian basement rock province (Blue Ridge province), Inner Piedmont province and the coastal plain (Carolina Slate province) [*Hatcher* 1989, *Taylor* 1989]. The western Appalachian foreland basin is generally associated with low velocity. The Brevard fault appears to be a major boundary that separates velocity highs to the west and a velocity low to the east. The region between the Brevard fault and the Central Piedmont show both low velocity and low isostatic gravity (Figure 1b, 9,10).

As noted earlier, a prominent low velocity anomaly interrupts the high velocity belt at the Tennessee-North Carolina border for both frequency bands. The spike tests (Figure 11) rules out the possibility of smearing of the low velocity present to north and south of the Appalachian Mountains. Also notice that the mountain chain and faults appear to bend dextrally near where the low velocity is present and then the strike returns to parallel the southern segment. The belt of Precambrian outcrop rock is very narrow at this segment but widens significantly northward and southward [*Reed & Harrison*, 1993]. This is also a region where the gravity is very low (Figure 1b). According to *Thomas* [2005], closing of the Impetus Ocean loaded much thicker clastic sediments into an embayment such as the Tennessee embayment than adjacent promontories. So we conjecture the low velocity anomaly present in this region may be a manifestation of the ancient Tennessee embayment at the Impetus Ocean margin. However, further investigations are necessary to determine its actual tectonic manifestation.

### 4.3 Gravity and Velocity Structure

The correlations between the isostatic gravity map (Figure 1b) and the velocity maps (Figure 9 and 10) are quite complex. In many cases the velocity is positively correlated with the gravity. For example for the Missouri batholith, southward extension of the Mid Continental rift, Wisconsin arch, Mississippi river arch as well as the region between Brevard fault and Central Piedmont suture, the low velocity is correlated with low gravity. The Appalachians west of Brevard fault, the linear feature at southern Alabama and northwestern Louisiana, the isolated velocity high in southern Georgia as well as for the velocity high in southwestern Texas, the high velocity is associated with a high gravity.

However, in other cases, velocity is negatively correlated with the isostatic gravity. The most obvious examples are the triple junction at the Texas and Oklahoma border, the central Piedmont Suture and the Atlantic coastal plain as well as the Reelfoot rift are featured as gravity highs but velocity lows. For those regions, the low velocities may be due to thick sediments. On the other hand, the north-south striking high velocity body east of the MCR is associated with a low gravity body.

## 4.4 Seismicity and velocity structure

High resolution P wave [*Vlahovic et al*., 2000] and S wave [*Vlahovic & Powell.*, 2001] tomographic studies have shown that the most of the NMSZ earthquakes are located in low P wave velocity zones. A strong low velocity anomaly is also observed in the NMSZ for 5 second period surface waves (Fig. 9). Rayleigh waves of this period sample almost the same depth range as the two body wave studies, although the body wave studies have much higher resolution than this study. Similar observations were also made in the two body wave studies. For T=15s, the NMSZ appears to separate a velocity high to the east and a velocity low to the west. The strong low velocity anomaly present to the west of the NMSZ is consistent with the large station residuals of teleseismic earthquakes for stations located to the west of the seismic zone as found by *Vlahovic et al*., [2000] and *Vlahovic & Powell*, [2001]. Similarly, the seismicity of the Wabash Valley seismic zone, the east-west striking Ouchita Orogen seismic zone as well as the Eastern Tennessee seismic zones are either located in relatively low velocity zones or transition zones (presumably weak in strength). Thus, the recent seismicity may be due to the reactivation of ancient tectonic structures. For example, the Eastern Tennessee and the Ouchita Orogen seismic zones may be related to the reactivation of the faults built along the Appalachian- Ouachita orogen, while the New Madrid and and Wabash Valley seismic zones may be related to the development of the Reelfoot rift, the Ozark uplift as well as the Illinois basin. A higher resolution study however is needed to determine the accurate fault geometry and their relationship to surrounding geologic units.

## 5. Conclusions.

High quality surface waves are extracted by cross-correlating the ambient noise data recorded by stations distributed in the eastern North America. As indicated by the relative strength of Pseudo-Green's Functions, the Atlantic Ocean dominates the Gulf of Mexico and the Pacific ocean in contributing to the ambient noise field in this region.

The group velocity map of 5 second surface waves is generally consistent with the near surface geology while that of 15 seconds surface waves is indicative of large scale regional tectonics. Regions with thick sediments are generally associated with low velocity, while regions with shallower depth to Precambrian basement are dominated by high velocities. The ancient rift zones are often associated with low velocity, such as the Triassic triple junction at the Oklahoma-Texas border, Mid-Continent Rift (MCR) in Lake Superior and its east limb and the Reelfoot rift in the eastern Mississippi embayment. Furthermore, our results provide additional evidence for the southward extension of the west-limb of the MCR from Kansas into western Oklahoma.

The Appalachian Mountains are characterized by a linear, high velocity anomaly (due to the upthrust of the Precambrian basement), except for the central part at the Tennessee-North Carolina border, where the low velocity anomaly may be indicative of the location of the ancient Tennessee embayment along the Impetus Ocean margin.

Surface wave group velocity is generally positively correlated with the isostatic gravity. However, for regions with heavy volcanic history and thick sediment coverage, such as the ancient rift zones, an anti-correlation is observed.

The seismic zones in New Madrid, Wabash Valley and Eastern Tennessee as well as the Ouchita Orogen Seismic Zone are approximately located in low velocity or transition zones. This observation may suggest that all of those major seismic zones are associated with the reactivation of ancient tectonic activities as a response to the present tectonic evolution.

**Acknowledgements**:

We thank Dr. Michel Campillo, Nikolai M. Shapiro for their kind help on the implementation of the cross-correlation method. We also thank Mitch Withers who helped us to acquire noise data and make this work possible. Arch Johnston and Bob Smalley provided useful comments on a draft of this paper. We also appreciate the valuable suggestions from two anonymous reviewers and the Associated Editor. This work was supported by the Center for Earthquake Research and Information (CERI), University of Memphis. This is the CERI contribution #518.

**Reference**:

Anderson, R. R. (1990). Interpretation of geophysical data over the Midcontinent Rift System in the area of the M. G. Eischeid #1 Petroleum Test, Carroll County, Iowa, in Anderson, R. R. ed., The Amoco M. G. Eischeid #1 deep petroleum test Carroll County, Iowa: Iowa department of Natural Resources Special Report Series No. 2, P. 27-38.

Adams, C. D., and G. R. Keller (1993). Possible extension of the Midcontinent Rift in west Texas and eastern New Mexico, *Can. J. Earth. Sci.*, *31*, 709-720.

Allen, D. J., W. J. Hinze and W. F. Cannon (1992). Drainage, topographic, and gravity anomalies in the lake Superior region: Evidence for a 1100 Ma mantle plume. *Geoph. Res. Let.*, *19*, 2118-2122.

Barmin, M. P., M. H. Ritzwoller, and A. L. Levshin (2001). A fast reliable method for surface wave tomography, *Pure. Appl. Geophys.*, *158*, 1351-1375.

Bassin, C., Laske, G. and Masters, G. (2000), The current limits of resolution for surface wave tomography in North America, EOS Trans AGU, 81, F897.

Bensen, G. D., M. H. Ritzwoller, M. P. Barmin, A. L. Levshin, F. Lin, M. P. Moschetti, N. M. Shapiro, and Y. Yang (2007), Processing seismic ambient noise data to obtain reliable broad-band surface wave dispersion measurements, *Geophys. J. Int.*, 169, 1239-1260, doi: 10.1111/j.1365-246X.2007.03374.x.

Berendsen, P., R. M. Borcherding, J. Doveton, et al (1988), Texaco Poersch #1, Washing County, Kansas-Preliminary geologic report of the pre-Phanerozoic rocks: Kansas Geological Survey Open File Report 88-22, 116p.

Braile, L. W., W. J. Hinze, R.R.B. von Frese, and G. R. Keller (1989). Seismic properties of the crust and uppermost mantle of the conterminous Unites States and adjacent Canada, *Geophysical Framework of the Continental United States, Geological Society of America Memoir 172*, 655-681.

Campillo, M., A. Paul (2003), Long-Range correlations in the diffuse seismic coda, *Science*, 299, 547-549.

Catchings, R., D., (1999), Regional Vp, Vs, Vp/Vs, and Poisson's ratios across earthquake source zones from Memphis, Tennessee, to St. Louis, Missouri, *Bull. Seism. Soc. Am.*, 89, 1591-1605.

Claerbout, J. F., Synthsis of a layered medium from its acoustic transmission response, *Geophys.*, 33, 264-269, 1968.

Collinson, C., M. L. Sargent, and J. R. Jennings (1988). The Illinois basin, *The Geology of North America, vol. D-2, Sedimentary cover-North America Craton: U.S.,The geological Society of America* 383-426.

Derode, Arnold, E. Larose, M. Campillo, M. Fink (2003), How to estimate the Green's Function of a heterogeneous medium between two passive sensors? Application to acoustic waves, *Appl. Phys. Lett.*, 83, 3054-3056.

Duval, T. L. Jr., S. M. Jefferies, J. W. Harvey, and M. A. Pomerantz (1993), Time-distance helioseismology, *Nature*, 362, 430-432.

Ervin, C. P., L. D. McGinnis (1975), Reelfoot rift: reactivated precursor of the Mississippi embayment, *Geological Society of American Bulletin*, 86, 1287-1295.

Gaherty, J. B. (2004). A surface wave analysis of seismic anisotropy beneath eastern North America, *Geophys. J. Int., 158*, 1053-1066.

Godey, S., R. Sneider, A. Villasenor, and H. M. Benz (2003). Surface wave tomography of North America and the Caribbean using global and regional broad-band networks: phase velocity maps and limitations of ray theory, *Geophys. J. Int., 152*, 620-632.

Gravity Anomaly Map Committee, (1987). Gravity Amomaly Map of North America (1:5,000,000). Boulder, Colorado, Geological Society of America, Continent-Scale Map-002(5 sheets).

Hatcher, R. D., Jr (1989). Appalachian introduction, *The Geology of North America, vol. F-2, Appalachian-Ouachita Orogen in the United States*, 1-6.

Herrin, E., and T. Goforth (1977). Phase-matched filters: Application to the study of Rayleigh waves, *Bull. Seism. Soc. Am.*, *67*, No. 5, 1259-1275.

Herrmann, R. B. (1973). Some aspects of band-pass filtering of surface waves, *Bull. Seism. Soc. Am.*, *63*, No. 2, 663-671.

Herrmann, R. B. and G. W. Fischer (1978). Theoretical seismogram constraints on some crustal velocity models in the central United States *PAGEOPH* 116**,** 1250-1261.

Herrmann, R. B. (1974). Surface wave generation by Central United States earthquakes, PHD *Dissertation*.

Hildenbrand, T. G., and J. D. Hendricks(1995). Geophysical setting of the reelfoot rift and relations between rift structures and the New Madrid seismic zone, *in Investigations of the New Madrid seismic zone, Shedlock, K. M., and A. Johnston eds. USGS Professional Paper 1538-E*, E1-E30.

Hinze, W. J., D. J. Allen, L. W. Braile, and J. Mariano (1997). The Midcontinent rift system: a major proterozoic continental rift, in Ojakangas, R. W., Dickas, A. B., and Green, J. C., eds., Middle Proterozoic to Cambrian Rifting, Central North America, *Geological Society of America Special paper 312*, 7-35.

Jachens, R. C., R. W. Simpson, and R. J. Blakely (1989). Isostatic residual gravity and crustal geology of the United States, *Geophysical Framework of the Continental United States, Geological Society of America Memoir 172*, 405-425.

Johnston, A. C. and E. S. Schweig (1996). The enigma of the New Madrid earthquakes of 1811-1812, *Annu. Rev. Earth Sci.*, 339-384.

Kane, M. F. and R. H. Godson (1989). A crust/mantle structural framework of the conterminous United States based on gravity and magnetic trends, *Geophysical Framework of the Continental United States, Geological Society of America Memoir 172*, 383-403.

Kearey, P., and F. J. Vine (2004), Global Tectonics, *Blackwell Science*

Langston, C. A., (1994), An integrated study of crustal structure and regional wave propagation for southeastern Missouri, *Bull. Seism. Soc. Am.*, 84, 105-118.

Langston, C. A. (2003), Local earthquake wave propagation through Mississippi embayment sediments, Part I: body wave phases and local site responses, *Bull. Seism. Soc. Am.*, 93, 2664-2684.

Larose, E., A. Derode, M. Campillo, and M. Fink (2004), Imaging from one-bit correlations of wideband diffuse wavefields, *J. Appl. Phys.*, 95, 8393-8399.

Levshin, A., L. Ratnikova, and J. Berger (1992). Peculiarities of surface-wave propagation across central Eurasia, *Bull. Seism. Soc. Am.*, *82*, No. 6, 2464-2493.

Liang, C., X.D. Song, J.L. Huang (2004), Tomographic Inversion of Pn Travel-Times in China, *J. Geophys. Res*., 109, B11304, doi. 10.1029/2003JB002789.

Lobkis, O. I., R. L. Weaver (2001). On the emergence of the Green’s function in the correlations of a diffuse field, *J. Acoust. Soc. Am.*, 110, 3011-3017.

Mitchell, B. J., R. B. Herrmann (1979). Shear velocity structure in the eastern United States from the inversion of surface wave group and phase velocities, *Bull. Seism. Soc. Am.*, *69*, No. 4, 1133-1148.

Mooney, W. D., M. C. Andrews, A. Ginzburg, A. A. Peters and R. M. Hamilton. (1983). Crustal structure of the northern Mississippi embayment and a comparison with other continental rift zone, *Tectonophysics*, *94*, 327-348.

Moschetti, M. P., M. H. Ritzwoller, and N. M. Shapiro (2007), Surface wave tomography of the western United States from ambient seismic noise: Rayleigh wave group velocity maps, *Geochem., Geophys., Geosys.*, 8, Q08010, doi:10.1029/2007GC001655.

Nixon, G. A. (1988). An analysis of geophysical anomalies in north-central Oklahoma and their relationship to the Midcontinent geophysical anomaly [M.S. thesis]. Norman, University of Oklahoma, *118p*.

Paige, C. C., M.A.Saunders (1982a), LSQR: An algorithm for sparse linear equations and least squares problems, ACM Transactions on Mathematical software, 8, No.1, 43-71

Paige, C. C., M.A.Saunders (1982b), LSQR: Sparse linear equations and least squares problems, ACM Transactions on Mathematical software, 8, No.2, 195-209.

Parkiser, L. C. and W. D. Mooney (1989) edit. *”Geophysical Framework of the Continental United States“, Geological Society of America Memoir 172*.

Phinney, R. L. and K. Roy-Chowdhury (1989). Reflection seismic studies of crustal structure in the eastern United States, *Geophysical Framework of the Continental United States, Geological Society of America Memoir 172*, 613-653.

Reed, J. C. and Harrison J. E (1993). Precambrian: Conterminous U. S., *Geological Society of America Memoir v. C-2*, 1-10.

Reed, J. C. Jr., and C. A. Bush, (2005), Generalized Geologic Map of the Conterminous United States: U.S. Geological Survey, Denver, CO.

Rickett, J., J. F. Claerbout (1999), Acoustic daylight imaging via spectral factorization: Helioseismology and reservoir monitoring, *The Leading Edge*, 18(8), 957-960.

Roux, P., K., G. Sabra, W. A. Kuperman, and A. Roux et. al (2005), Ambient noise crosscorrelation in free space: Theoretical approach., *J. Acoust. Soc. Am.*, 117, 79-84.

Roux, P., W. A. Kuperman and NPAL Group (2004), Extracting coherent wavefronts from acoustic ambient noise in the ocean, *J. Acoust. Soc. Am.*, 116, 1995-2003.

Sabra, K. G., P. Gerstoft, P. Roux, and W. A. Kuperman (2005a), Extracting time-domain Green function estimates from ambient seismic noise, *Geophys. Res. Lett.*, 32, L03310, doi: 10.1029/2005GL021862.

Sabra, K. G., P. Gerstoft, P. Roux, and W. A. Kuperman (2005b), Surface wave tomography from microseisms in Southern California, *Geophys. Res. Le*tt., 32, L14311, doi: 10.1029/2005GL023155.

Shapiro, N. M., and M. Campillo (2004), Emergence of broadband Rayleigh waves from correlations of the ambient seismic noise, *Geophys. Res. Le*tt., 31, L07614, doi: 10.1029/2004GL019491.

Shapiro, N. M., M. Campillo, L. Stehly and M. H. Ritzwoller (2005), High-resolution surface wave tomography from ambient noise, *Science*, 307, 1615-1618.

Snieder, R., A., G. H. Douma and J. Scales (2002), Coda wave interferometry for estimating nonlinear behavior in seismic velocity, *Science*, 295, 2253-2255.

Snieder, R., A. (2004), Extracting the Green’s function from the correlation of coda waves: a derivation based on stationary phase, *Physical Review*, 69, 046610-1-8.

Stark, T. J. (1997). The east continent rift complex: evidence and conclusions, in Ojakangas, R. W., Dickas, A. B., and Green, J. C., eds., Middle Proterozoic to Cambrian Rifting, Central North America, *Geological Society of America Special paper 312*, 253-285.

Taylor, S. (1989). Geophysical framework of the Appalachians and adjacent Grenville province, in *Geophysical Framework of the Continental United States, Geological Society of America Memoir 172*, 317-348.

Thomas, W. A. (2005). Tectonic Inheritance at a Continental Margin, *GSA Today 16, No 2*, 4-11 doi. 10.1130/1052-5173(2006)016.

van der Lee, S. and G. Nolet (1997). Upper mantle S velocity structure of North America, *J. Geophys. Res.*, *102*, B10, 22,815-22,838.

van der Voo, R. (1989). Paleomagnetism of North America; The craton, its margins, and the Appalachian belt, *Geophysical Framework of the Continental United States, Geological Society of America Memoir 172*, 447-470.

Villasenor, A., Y. Yang, M. H. Ritzwoller, and J. Gallart (2007), Ambient noise surface wave tomography of the Iberian Peninsula: Implications for shallow seismic structure, *Geophys. Res. Lett.,* 34, L11304, doi:10.1029/2007GL030164.

Vlahovic, G., and C. A. Powell (2001). Three-dimensional S wave velocity structure and Vp/Vs ratio in the New Madrid seismic zone, *J. Geophys. Res., 106*, B7, 13,501-13,513.

Vlahovic, G., C. A. Powell, and J-M. Chiu (2000). Three-dimensional P wave velocity structure in the New Madrid seismic zone, *J. Geophys. Res.*, *105*, B4, 7999-8011.

Wapenaar, K., (2004), Retrieving the elastodynamic Green's function of an arbitrary inhomogeneous medium by cross correlation., *Phys. Rev. Lett.*, 93, 254301-1, 2004.

Weaver, Richard L., O I., Lobkis (2001), Ultrasonic without a source: Thermal fluctuation correlations at MHz frequencies, *Phys. Rev. Lett.*, 87, 134301.

Yang, Y., M. H. Ritzwoller, A. L. Levshin, and N. M. Shapiro (2007), Ambient noise Rayleigh wave tomography across Europe, *Geophys. J. Int.*, 168(1), page 259-274.

Yao, H., R. D. vander Hilst, M. V. de Hoop (2006), Surface-wave array tomography in SE Tibet from ambient seismic noise and two-station analysis –I. Phase velocity maps, *Geophys. J. Int.*, 166, 732-744.

Yarger, H. L. (1985), Kansas basement study using spectrally filtered aeromagnetic data, *in Hinze, W. J., ed., The utility of regional gravity and magnetic anomaly maps: Tusa, Oklahoma, Society of Exploration Geophysicists, 213-232*.

Zelt, C. A. (1998), Lateral velocity resolution from 3-D seismic refraction data, *Geophys. J. Int.*, 135, 1101-1112.

**Figure captions:**

**Figure 1a**, Station distribution and regional geology of eastern North America. The 24 solid triangles, 10 open triangles, 11 red pluses and 10 black pluses are stations belong to the United States National Seismic Network (USNSN), the NMSZ integrated regional network, NMSZ local network and the ETSZ network, respectively. Major faults are plotted as thin magenta lines. The thick brown lines lineate the major ancient rift zones. The Mid continent rift and the triple junction lines are digitized from the gravity map. The abbreviations are: OA=Oklahoma Aulacogen, RR=Reelfot Rift, ND=Nashville Dome, CA=Cincinnati Arch, BWB, Black Warrior Basin, IB=Illinois Basin. Major geological units are: Q=Quaternary deposit, nT=Neogene sedimentary rocks, pgT=Paleogene sedimentary rocks, K=Cretaceous, uPa=Upper Paleozoic sedimentary rocks, mPa=Middle Paleozoic sedimentary rocks, lPa=Lower Paleozoic sedimentary rocks, uPr=Upper proterozoic. The geologic data is compiled by *Reed and Bush* [2005] and can be downloaded from: http://pubs.usgs.gov/atlas/geologic/.

**Figure 1b**, Regional isostatic gravity (*Gravity Anomaly Map Committee,* 1987) and seismicity. The gravity is averaged within an 0.5° by 0.5° area. The black dots are seismicity. Major seismic zones include: NMSZ=New Madrid seismic zone, WVSZ=Wabash valley seismic zone, ETSZ=Eastern Tennessee seismic zone and the Ouachita Orogen seismic zone. Missouri Bath= Missouri Batholiths; Other abbreviations are the same as Figure 1a. The isostatic gravity data is downloaded from National

Geophysical Data Center (NGDC) at: http://www.ngdc.noaa.gov/. The seismicity is downloaded from USGS online earthquake center at: http://earthquake.usgs.gov/eqcenter/.

**Figure 2** Upper panel show the Cross Correlation Functions (CCFs) of station pair WVT-SLM. The 6 vertical lines mark the predicted time for P, S and Rayleigh (R) waves on negative and positive sides, respectively. The number on the left of each CCF is the date. Notice the surface waves dominate the CCFs and the directionality of Pseudo-GFs change with time. The CCFs in light gray show no apparent surface waves around the predicted times. The other CCFs are stacked and are shown in the lower panel.

**Figure 3**. CCFs arranged by distances of station pairs (with filter band 0.05-0.1 HZ). The main surface wave trains are observable for distance up to 2000 km. For better appearance, only one CCF per 80 km is plotted.

**Figure 4**. CCFs for period band between 2.5s and 7.5s arranged by azimuths of station pairs. Notice for CCFs with azimuth less than 180 degrees, GFs are dominantly strong on positive side. For CCFs with azimuth greater than 180 degrees, GFs are dominantly strong on negative side. Same pattern is observed for period band between 10s and 20s. This suggests the dominant noise sources is from east, possibly from Atlantic ocean.

**Figure 5**. FTAN method and phase equalization applied to the PGF of station pair AAM-RSSD. (a) Original wave form (blue) and the wave form after the phase-equalization process (red); (b) phase-equalized wave form (blue) and its tapered version (red); (c)

original FTAN spectrum; (d) FTAN spectrum after the phase equalization. Red triangles are local maxima automatically found by program.

**Figure 6a** Ray paths used in inversion for T=15.0 seconds.

**Figure 6b**, Group time-distance curves for period T=5.0 seconds (gray pluses) and T=15.0 seconds (black dots). The average group velocities determined by the inverse of the slope of the two fitted lines are 2.9km/s and 3.10km/s for T=5.0 and T=15.0 seconds, respectively. Notice the data for T=5.0 seconds ranging from 100km to 1500km degree while data for T=15.0 seconds ranging from 400 to 2000 degrees.

**Figure 7a** Checkerboard test for T=5.0 seconds with pattern size $1.5^\circ \times 1.5^\circ$. The white thick curve is the contour with resolvability equal to 0.7. The region enclosed by this curve is defined to be resolvable for pattern size equal to or larger than $1.5^\circ \times 1.5^\circ$ because the resolvability is larger than 0.7 (see text for details).

**Figure 7b** Resolution map for T=5.0 seconds surface wave tomography. Units are in degree. R=1.0x1.0 means the smallest size resolvable in this region is 1.0x1.0 degree.

**Figure 8a** Checkerboard test for T=15.0 seconds with pattern size $3.0^\circ \times 3.0^\circ$. Same as Figure 7a, except that this test is for period T=15 seconds, and the pattern size is $3.0^\circ \times 3.0^\circ$. Also notice the study region is larger than T=5 seconds.

**Figure 8b**, The resolution map for T=15 seconds. Same as the figure 7b, except that this is for period T=15 seconds.

**Figure 9** Group velocity map for Period T=5.0 seconds. The back and white lines are state boundaries and geological boundaries, respectively. The gray dots are earthquakes with magnitude larger than 3.0 from  1974 to 2004.

**Figure 10** Group velocity map for Period T=15.0 seconds. The back and magenta lines are state boundaries and faults, respectively. The gray dots are earthquakes with magnitude larger than 3.0 from  1974 to 2004.

**Figure 11** Spike test for Period T=15.0 seconds. The synthetic travel times are computed based on a synthetic model that consists of a background model with a constant velocity 3.1km/s and some localized low velocity spikes with a velocity of 2.8km/s (doted grids). The inverted model is shown in this figure.

Figure 1a

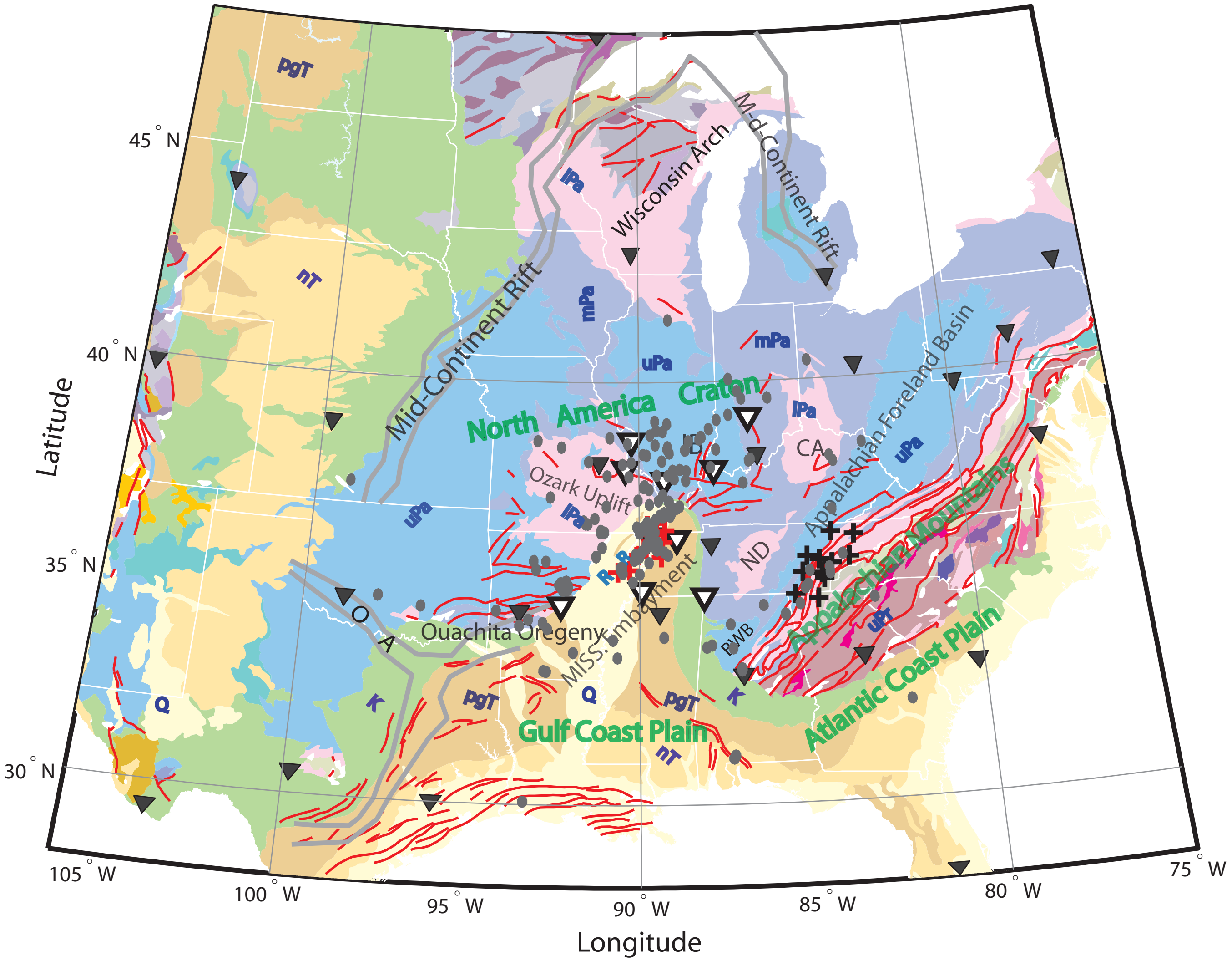
PgT
nT
lPa
mPa
uPa
mPa
lPa
uPa
uPa
lPa
Q
K
PgT
Q
PgT
K
nT
uPt
Mid-Continent Rift
Wisconsin Arch
Mid-Continent Rift
North America Craton
Ozark Uplift
IB
CA
Appalachian Foreland Basin
Appalachian Mountains
ND
RR
PWB
OA
Ouachita Oregeny
MISS. Embayment
Gulf Coast Plain
Atlantic Coast Plain
45° N
40° N
35° N
30° N
105° W
100° W
95° W
90° W
85° W
80° W
75° W
Latitude
Longitude

Figure 1b

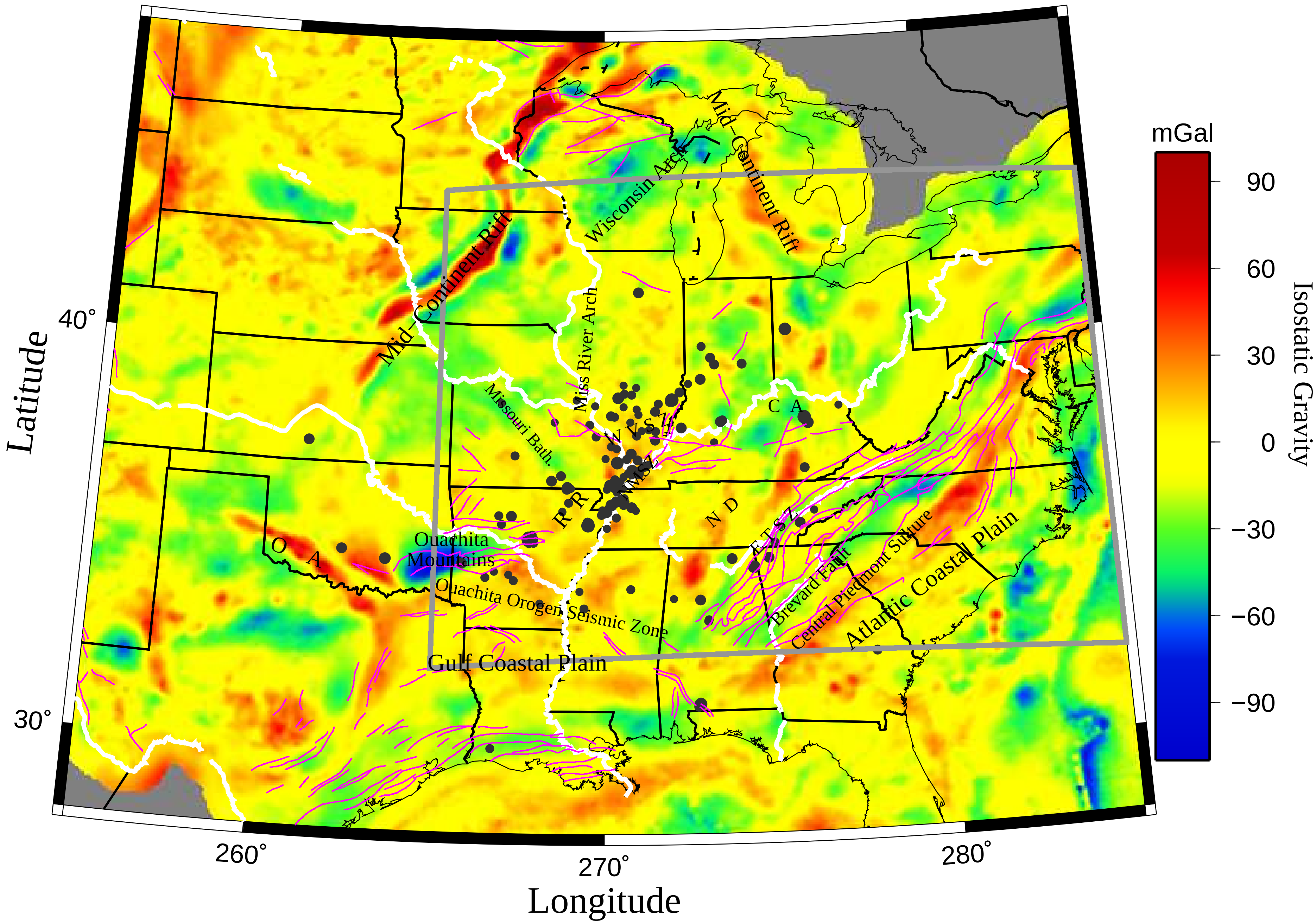
mGal
90
60
30
0
−30
−60
−90
Isostatic Gravity
Latitude
40°
30°
Longitude
260°
270°
280°
Mid−Continent Rift
Wisconsin Arch
Mid−Continent Rift
Miss River Arch
Missouri Bath.
N V S Z
NMSZ
R R
C A
N D
E T S Z
Ouachita Mountains
O A
Ouachita Orogen Seismic Zone
Brevard Fault
Central Piedmont Suture
Atlantic Coastal Plain
Gulf Coastal Plain

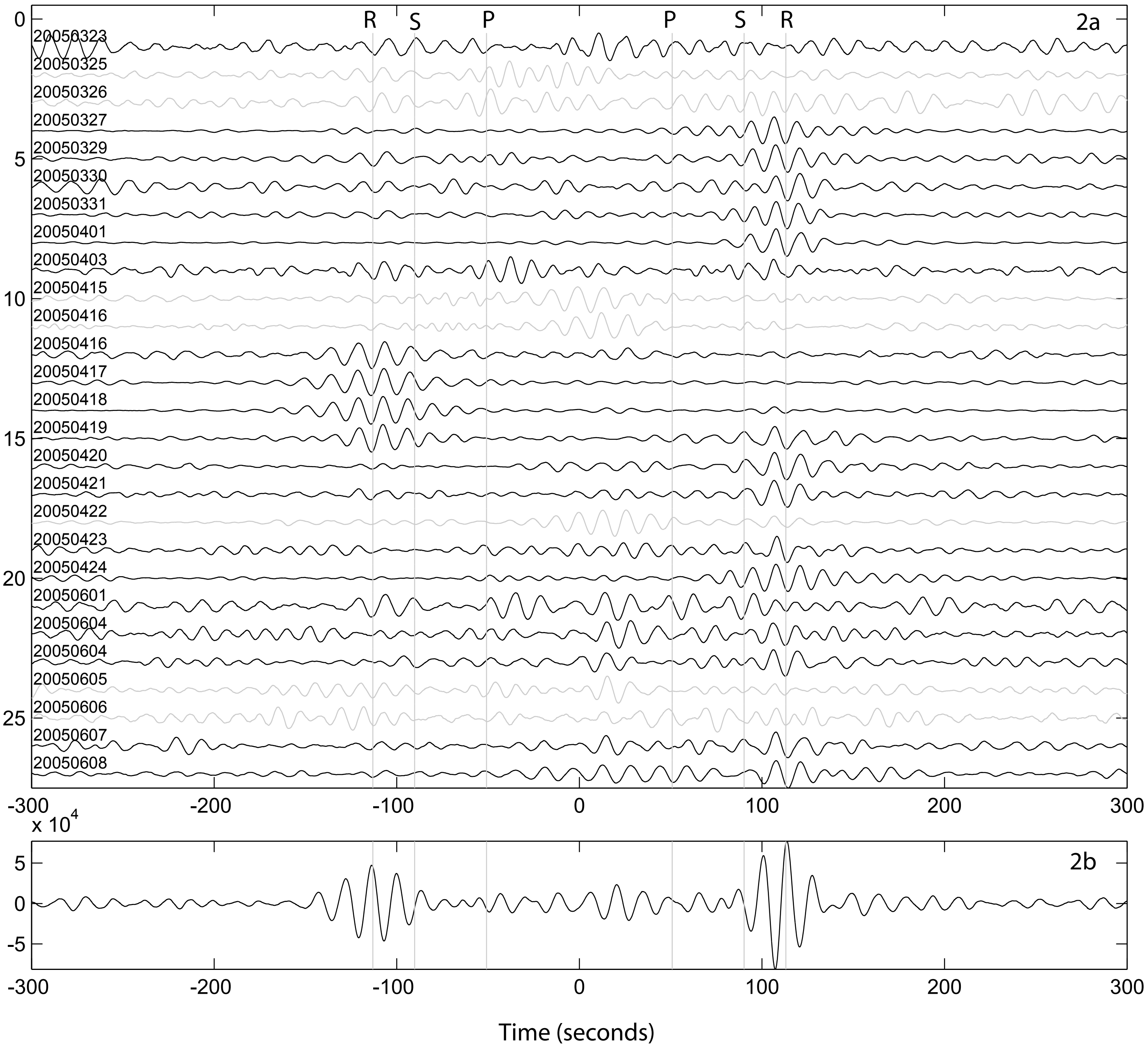
2a
R
S
P
P
S
R
20050323
20050325
20050326
20050327
20050329
20050330
20050331
20050401
20050403
20050415
20050416
20050416
20050417
20050418
20050419
20050420
20050421
20050422
20050423
20050424
20050601
20050604
20050604
20050605
20050606
20050607
20050608
0
5
10
15
20
25
-300
-200
-100
0
100
200
300
x $10^4$
2b
5
0
-5
-300
-200
-100
0
100
200
300
Time (seconds)

Figure 3

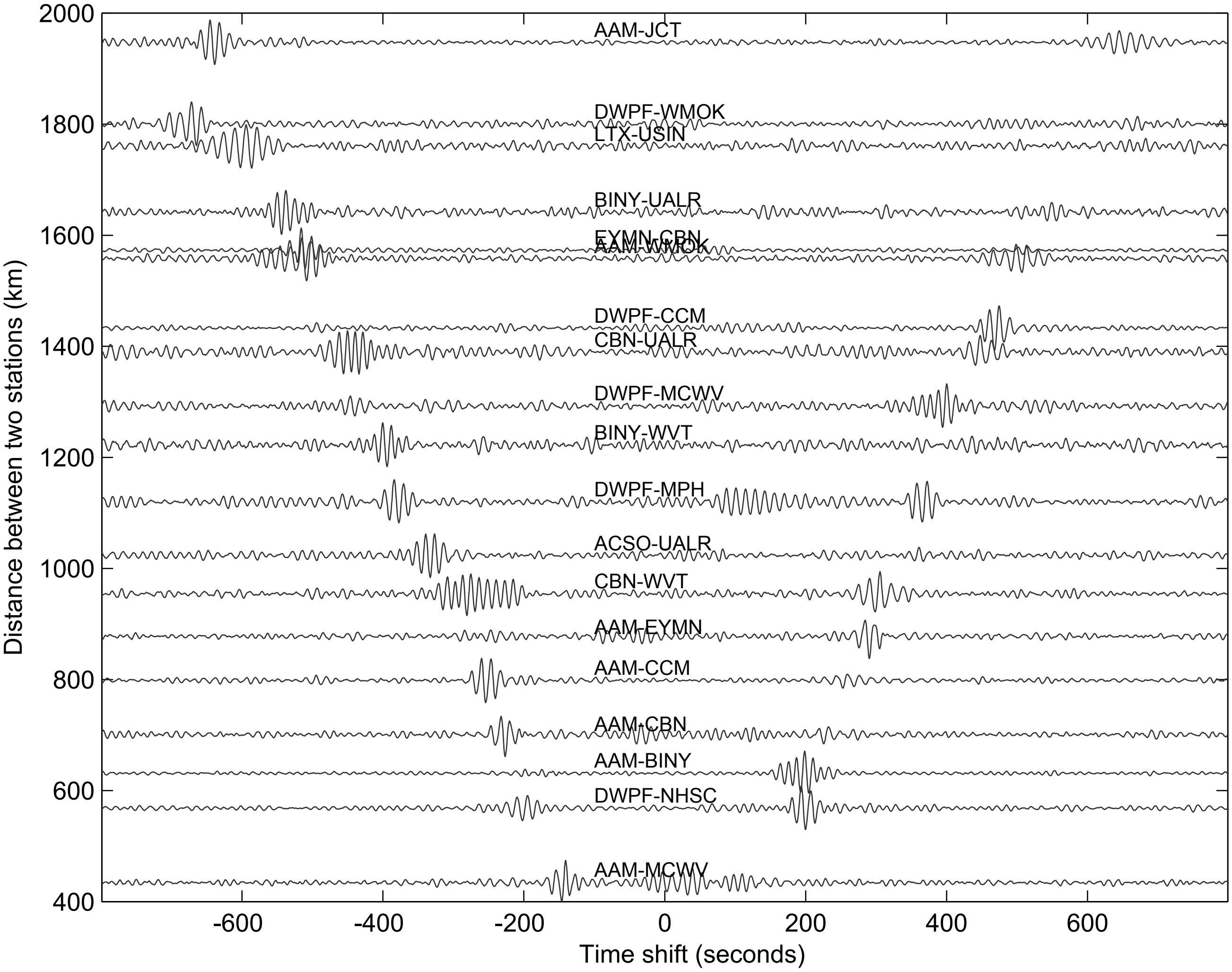
AAM-JCT
DWPF-WMOK
LTX-USIN
BINY-UALR
EYMN-CBN
AAM-WMOK
DWPF-CCM
CBN-UALR
DWPF-MCWV
BINY-WVT
DWPF-MPH
ACSO-UALR
CBN-WVT
AAM-EYMN
AAM-CCM
AAM-CBN
AAM-BINY
DWPF-NHSC
AAM-MCWV
2000
1800
1600
1400
1200
1000
800
600
400
Distance between two stations (km)
-600
-400
-200
0
200
400
600
Time shift (seconds)

Figure 4

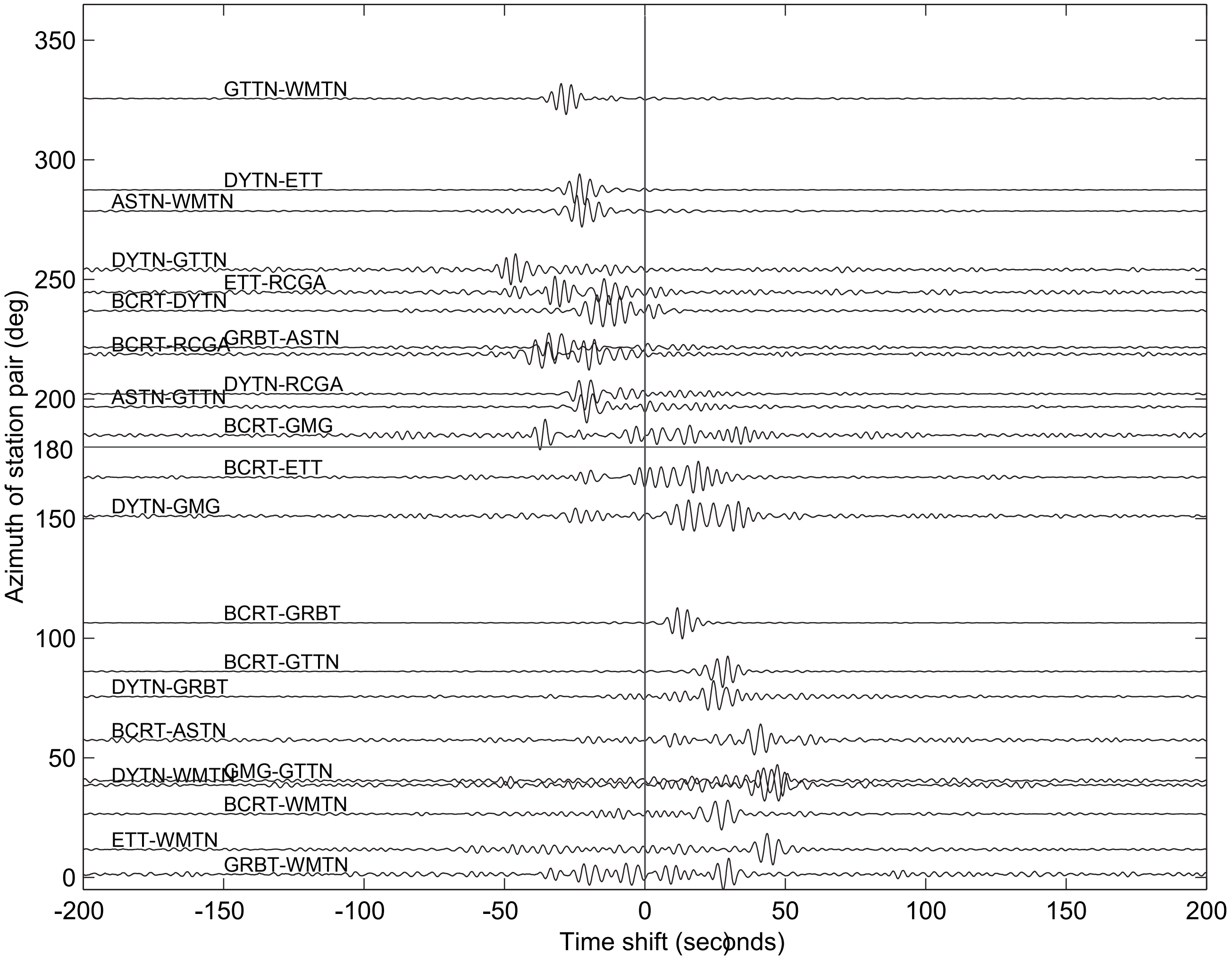
GTTN-WMTN
DYTN-ETT
ASTN-WMTN
DYTN-GTTN
ETT-RCGA
BCRT-DYTN
BCRT-RCGA
GRBT-ASTN
DYTN-RCGA
ASTN-GTTN
BCRT-GMG
BCRT-ETT
DYTN-GMG
BCRT-GRBT
BCRT-GTTN
DYTN-GRBT
BCRT-ASTN
DYTN-WMTN
GMG-GTTN
BCRT-WMTN
ETT-WMTN
GRBT-WMTN
350
300
250
200
180
150
100
50
0
Azimuth of station pair (deg)
-200
-150
-100
-50
0
50
100
150
200
Time shift (seconds)

Figure 5

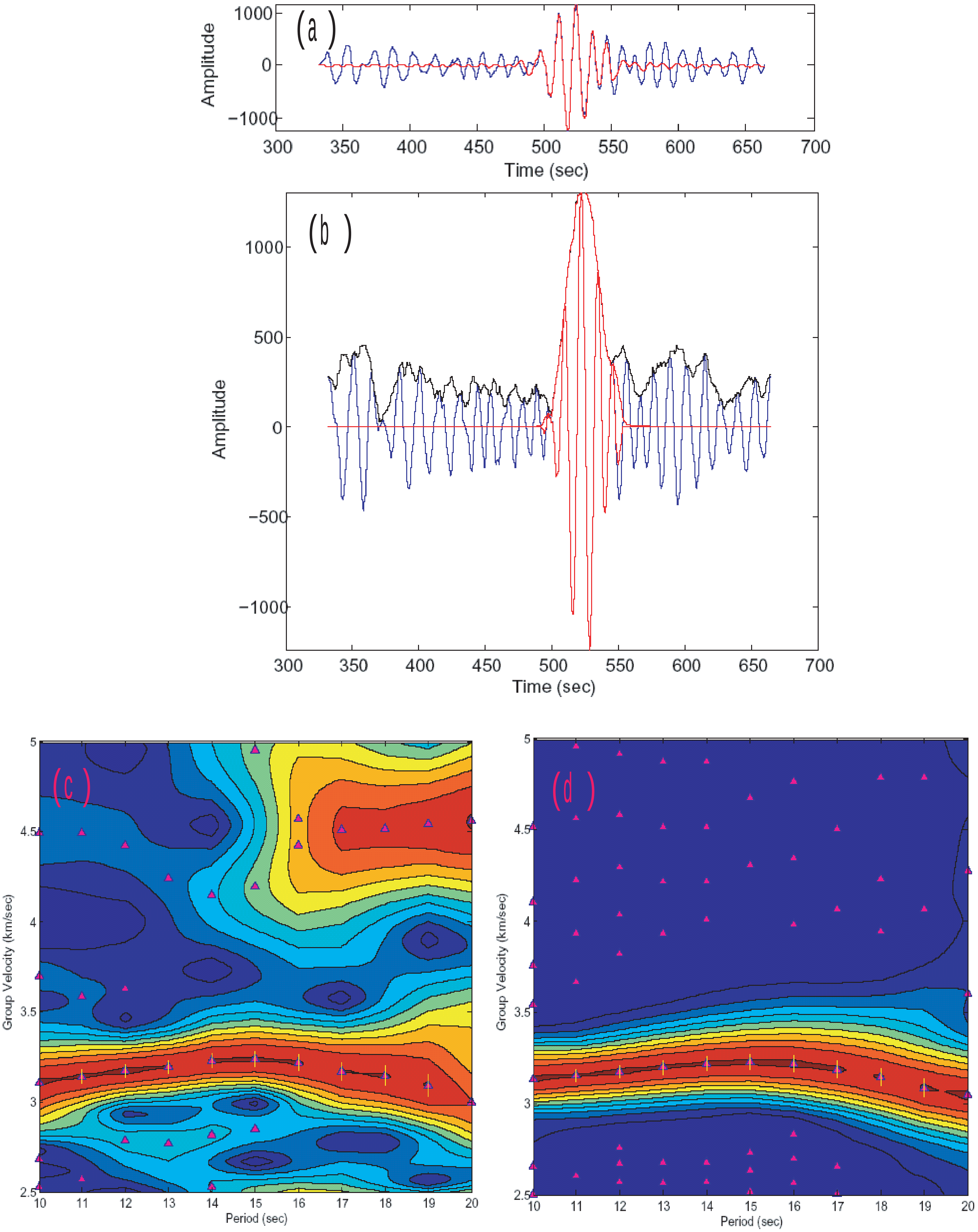
(a)
Amplitude
1000
0
−1000
300
350
400
450
500
550
600
650
700
Time (sec)
(b)
Amplitude
1000
500
0
−500
−1000
300
350
400
450
500
550
600
650
700
Time (sec)
(c)
Group Velocity (km/sec)
5
4.5
4
3.5
3
2.5
10
11
12
13
14
15
16
17
18
19
20
Period (sec)
(d)
Group Velocity (km/sec)
5
4.5
4
3.5
3
2.5
10
11
12
13
14
15
16
17
18
19
20
Period (sec)

Figure 6a

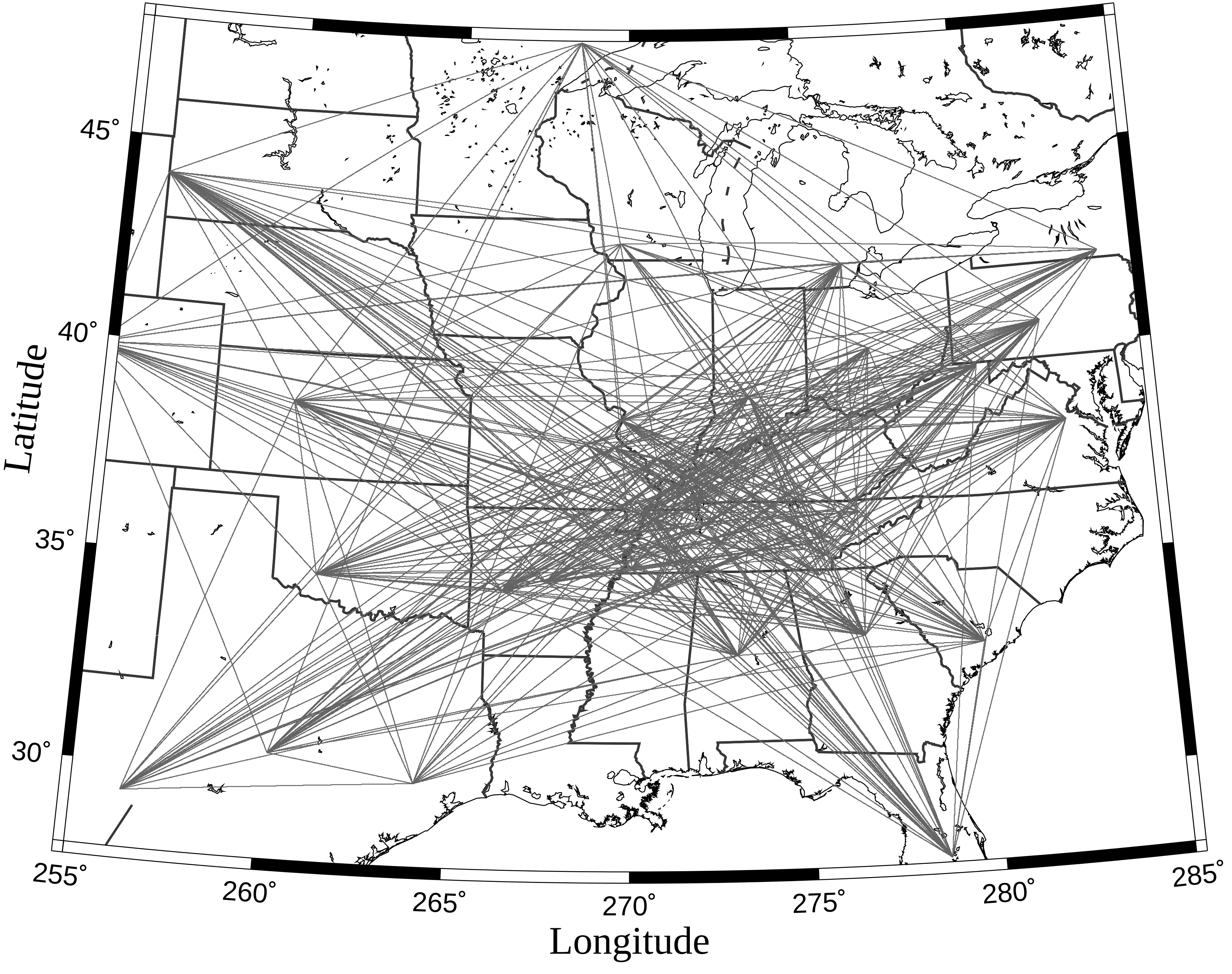

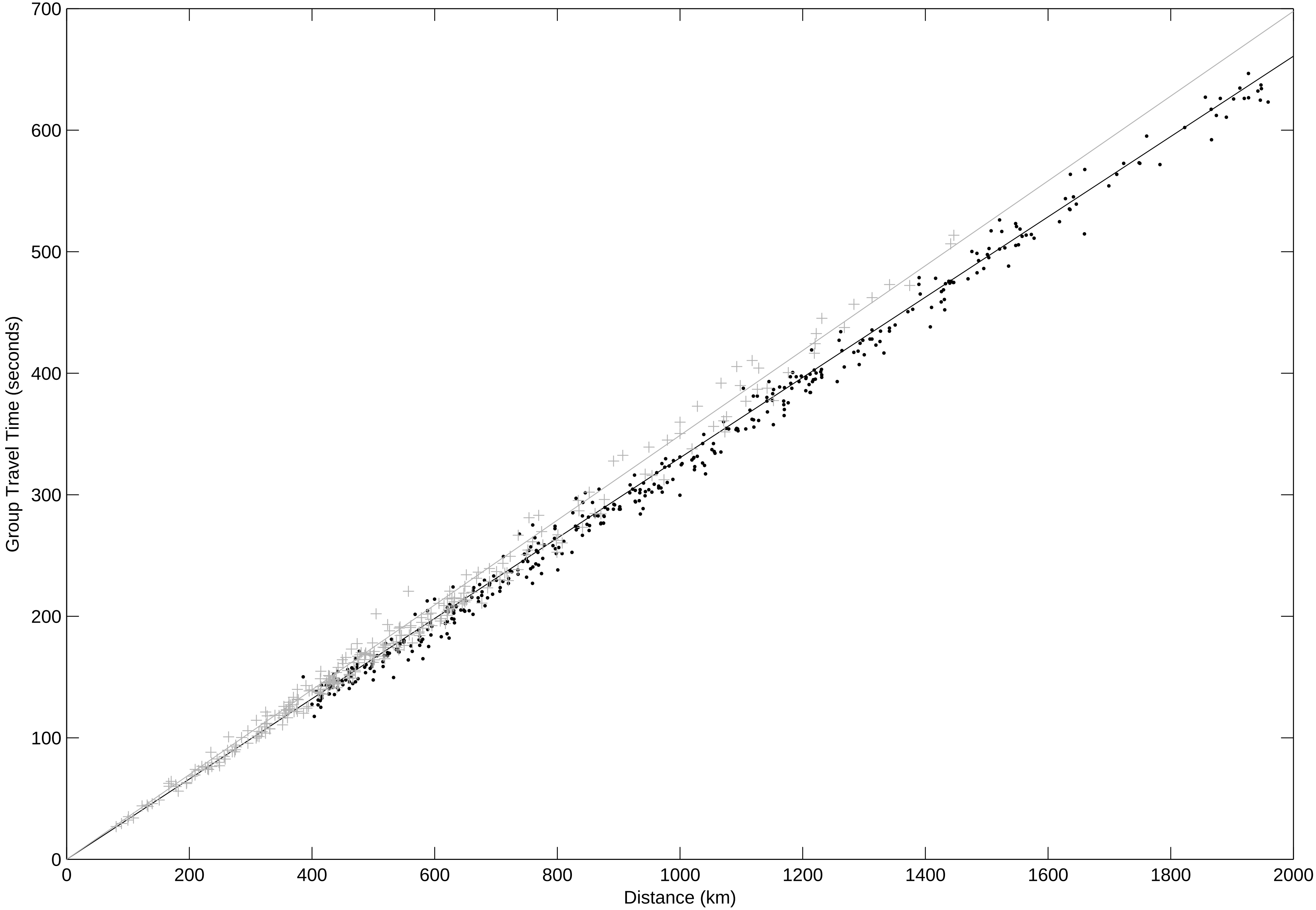
Group Travel Time (seconds)
Distance (km)
0
100
200
300
400
500
600
700
0
200
400
600
800
1000
1200
1400
1600
1800
2000

Figure 7a

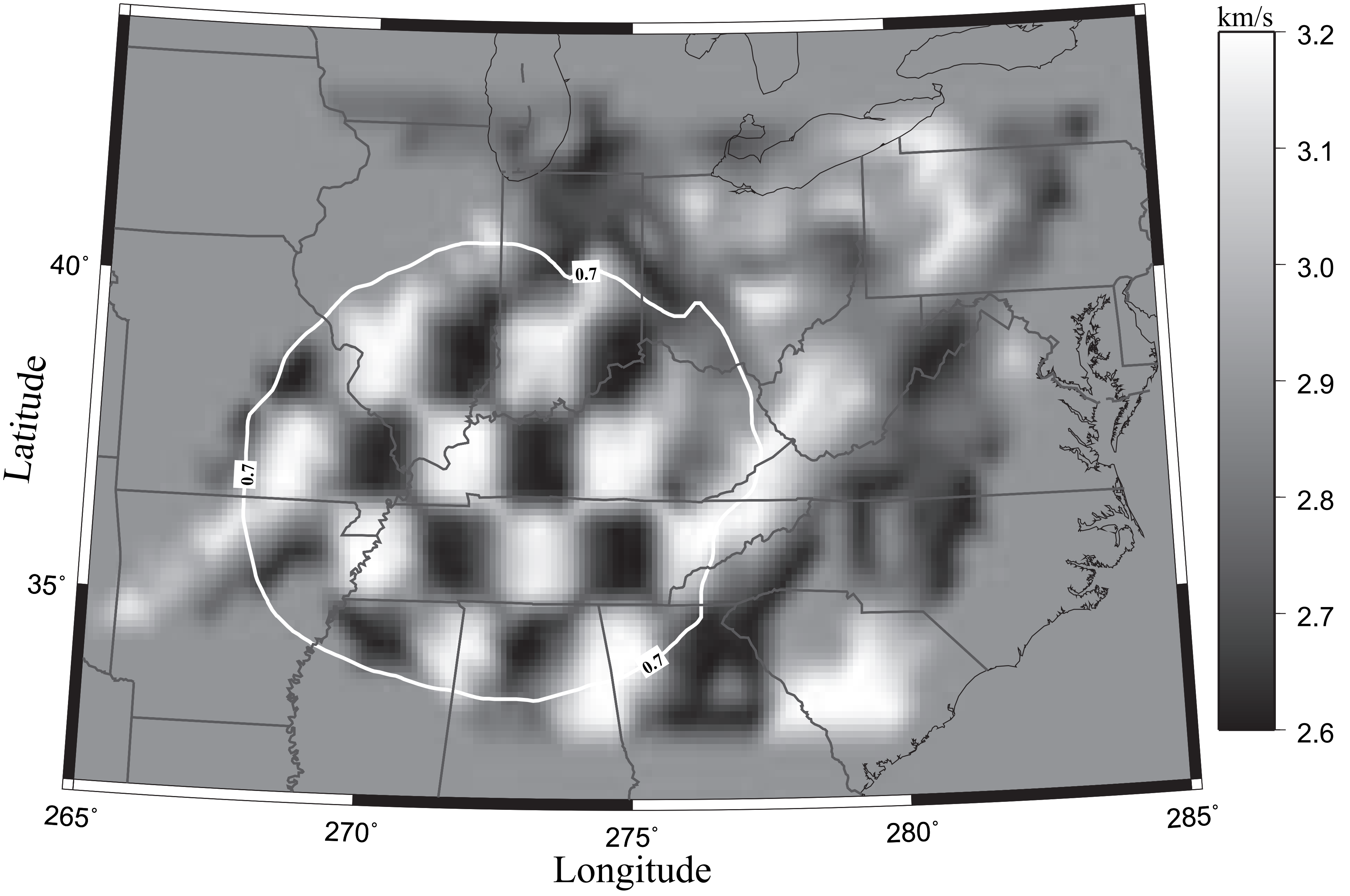
km/s
3.2
3.1
3.0
2.9
2.8
2.7
2.6
0.7
0.7
0.7
Latitude
40°
35°
265°
270°
275°
280°
285°
Longitude

Figure 7b

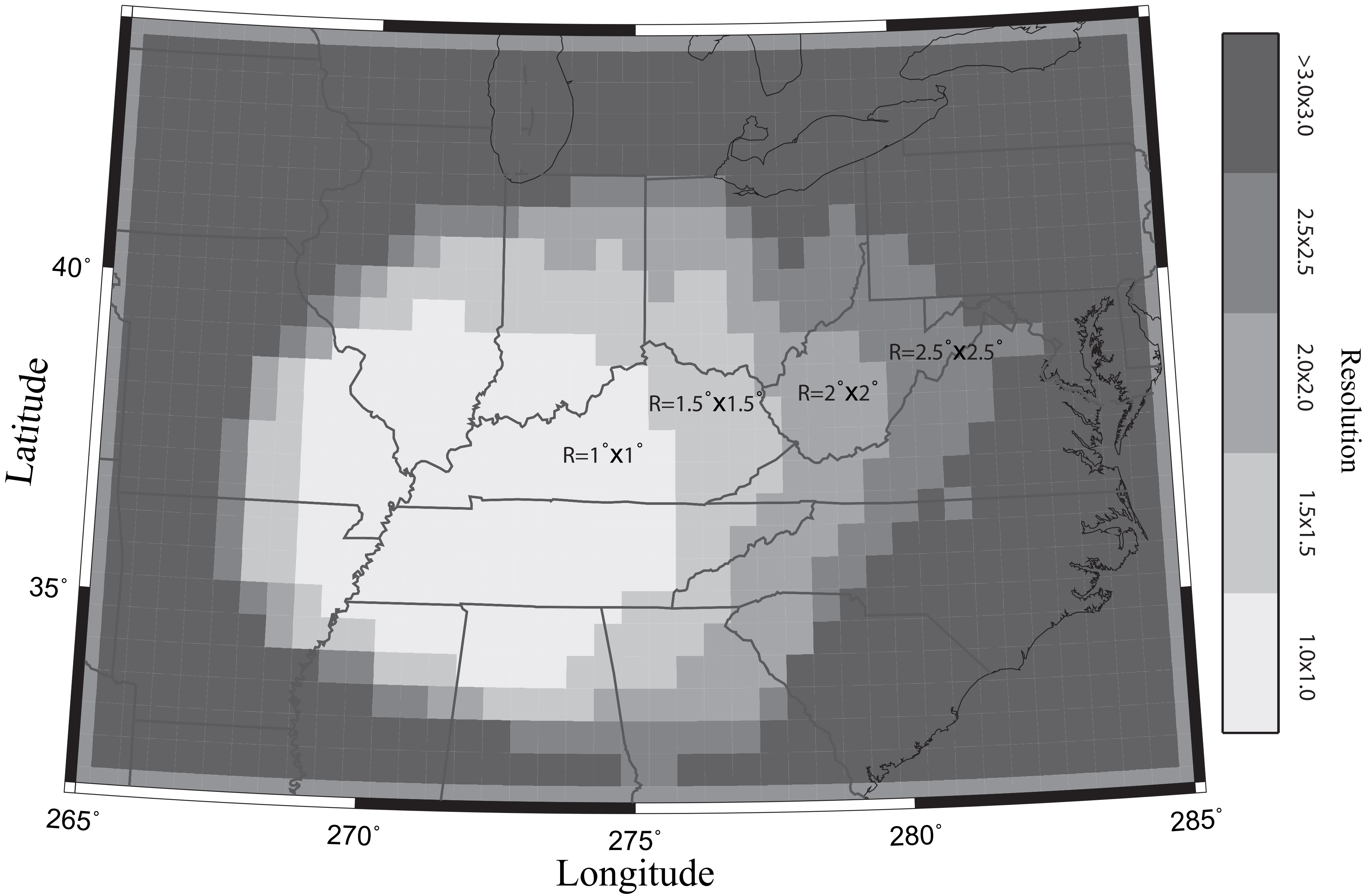
Latitude
40°
35°
Longitude
265°
270°
275°
280°
285°
R=1°x1°
R=1.5°x1.5°
R=2°x2°
R=2.5°x2.5°
Resolution
>3.0x3.0
2.5x2.5
2.0x2.0
1.5x1.5
1.0x1.0

Figure 8a

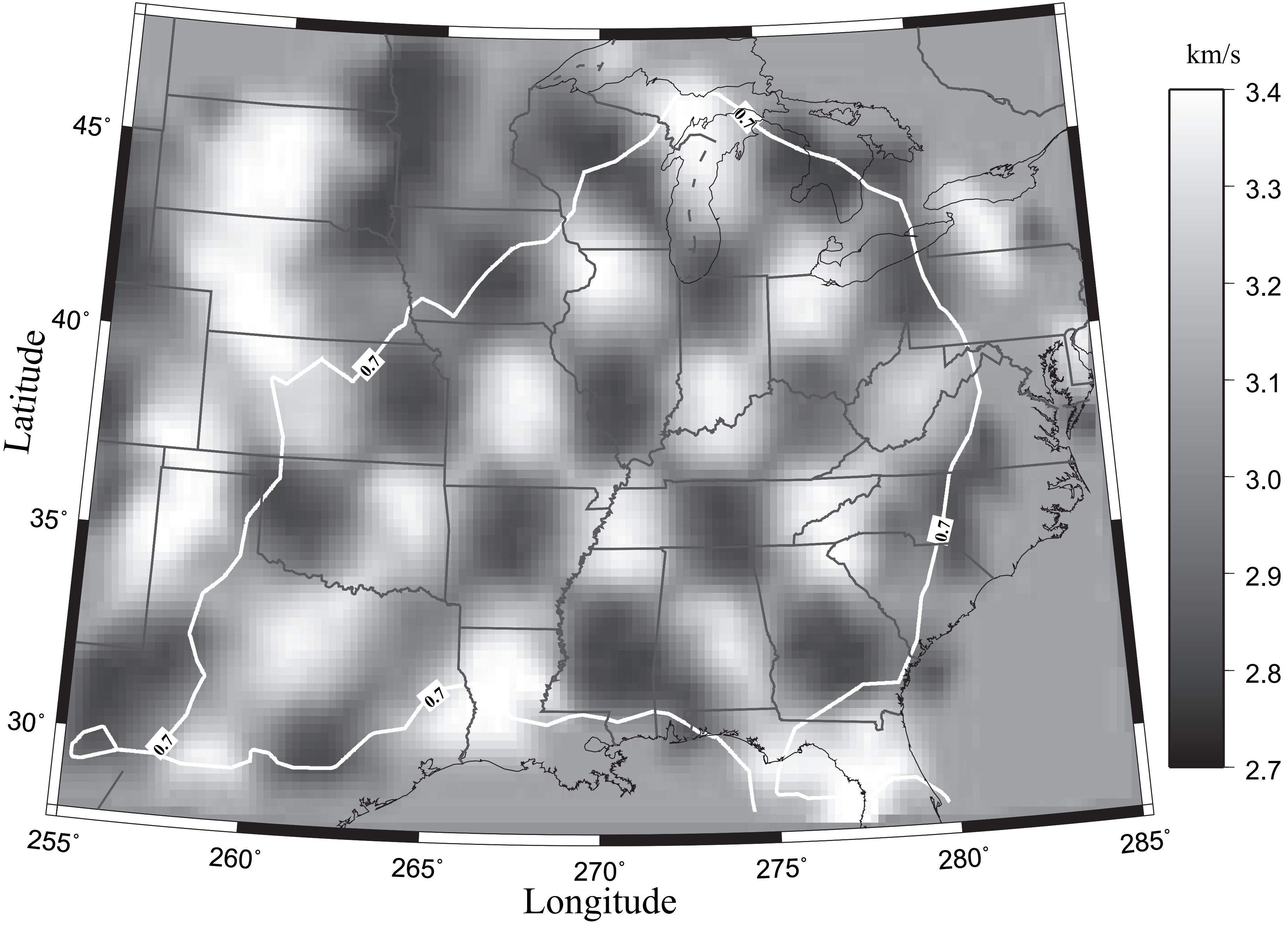

km/s
3.4
3.3
3.2
3.1
3.0
2.9
2.8
2.7
45°
40°
35°
30°
Latitude
255°
260°
265°
270°
275°
280°
285°
Longitude
0.7
0.7
0.7
0.7
0.7

Figure 8b

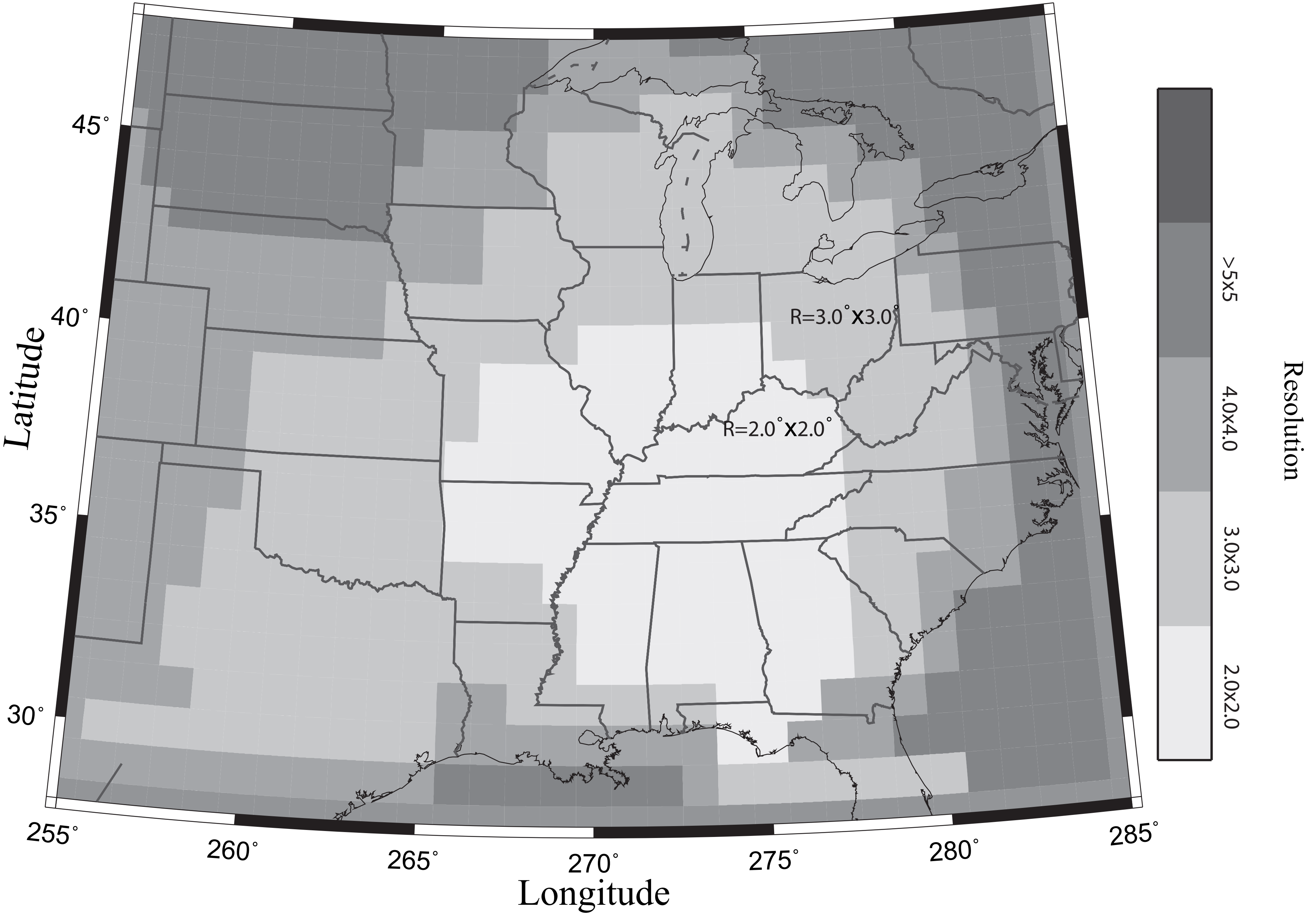

R=3.0° x3.0°
R=2.0° x2.0°
Latitude
45°
40°
35°
30°
Longitude
255°
260°
265°
270°
275°
280°
285°
Resolution
>5x5
4.0x4.0
3.0x3.0
2.0x2.0

Figure 9

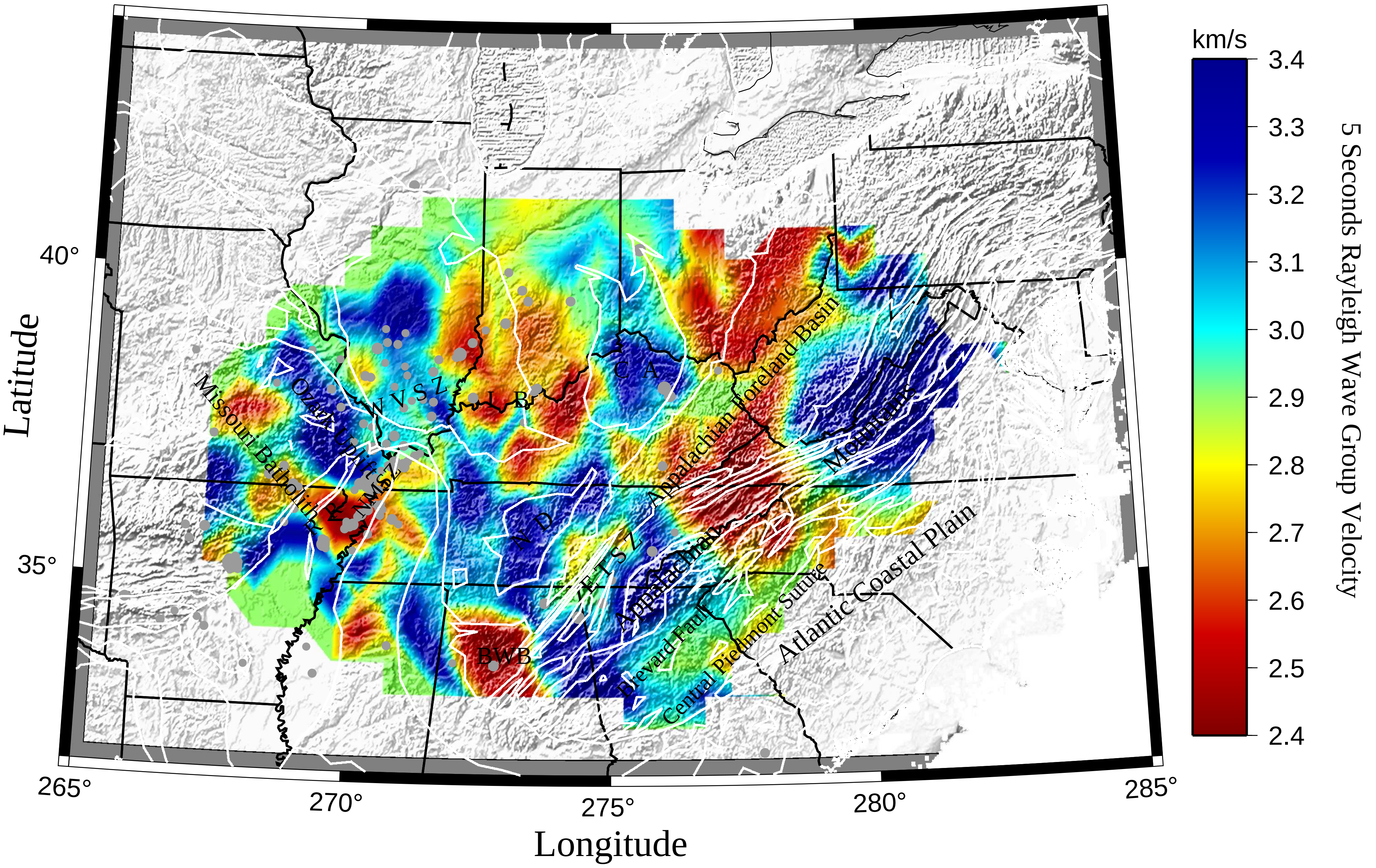
Latitude
40°
35°
Longitude
265°
270°
275°
280°
285°
km/s
3.4
3.3
3.2
3.1
3.0
2.9
2.8
2.7
2.6
2.5
2.4
5 Seconds Rayleigh Wave Group Velocity
Missouri Batholith
Ozark Uplift
W V S Z
L B
C A
R
N M S Z
N D
E T S Z
BWB
Appalachian Foreland Basin
Mountains
Appalachian
Brevard Fault
Central Piedmont Suture
Atlantic Coastal Plain

Figure 10

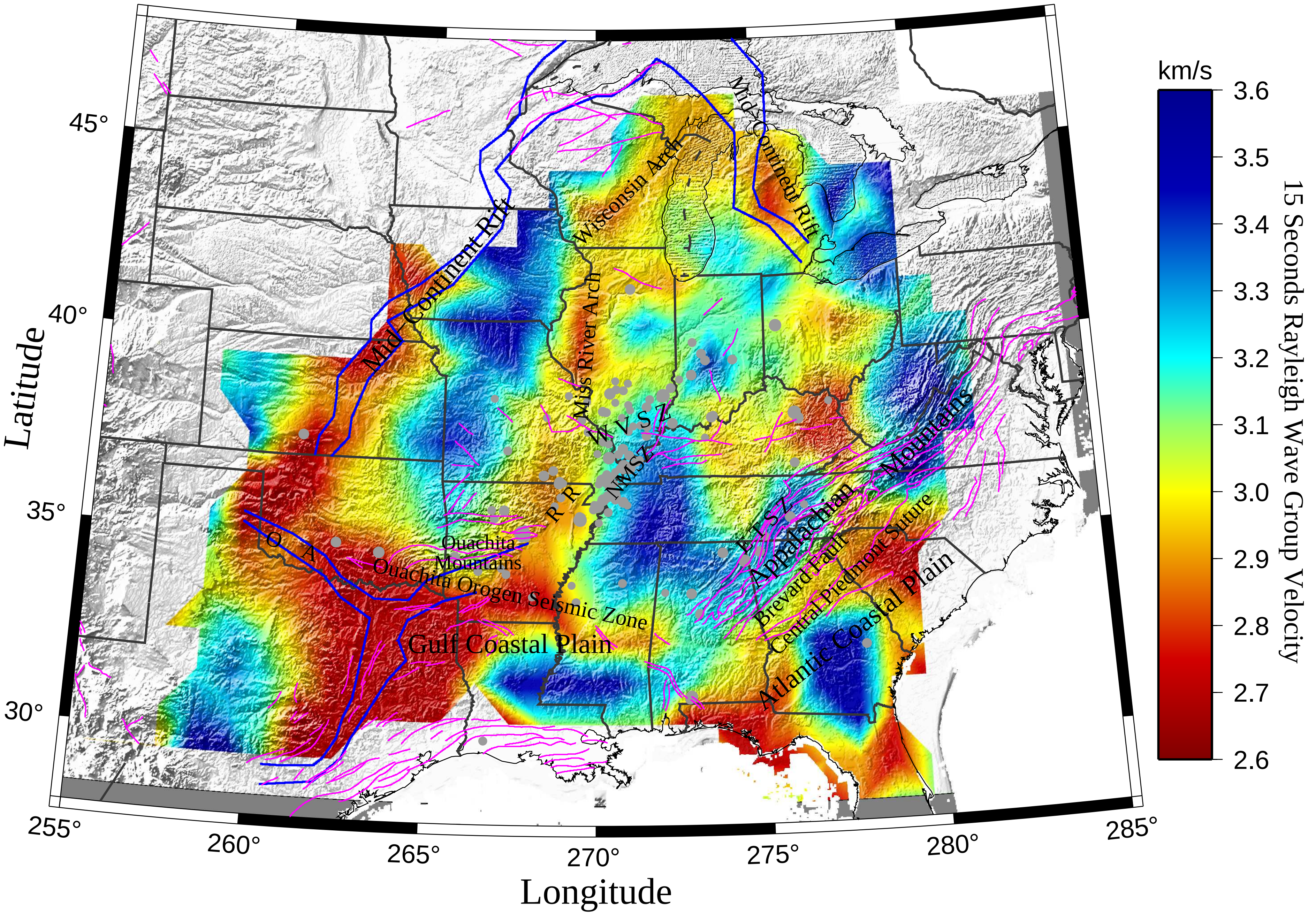
km/s
3.6
3.5
3.4
3.3
3.2
3.1
3.0
2.9
2.8
2.7
2.6
15 Seconds Rayleigh Wave Group Velocity
Latitude
45°
40°
35°
30°
Longitude
255°
260°
265°
270°
275°
280°
285°
Mid-Continent Rift
Mid-Continent Rift
Wisconsin Arch
Miss River Arch
W V S Z
NMSZ
R R
O A
Ouachita Mountains
Ouachita Orogen Seismic Zone
Gulf Coastal Plain
E T S Z
Appalachian Mountains
Brevard Fault
Central Piedmont Suture
Atlantic Coastal Plain

Figure 11

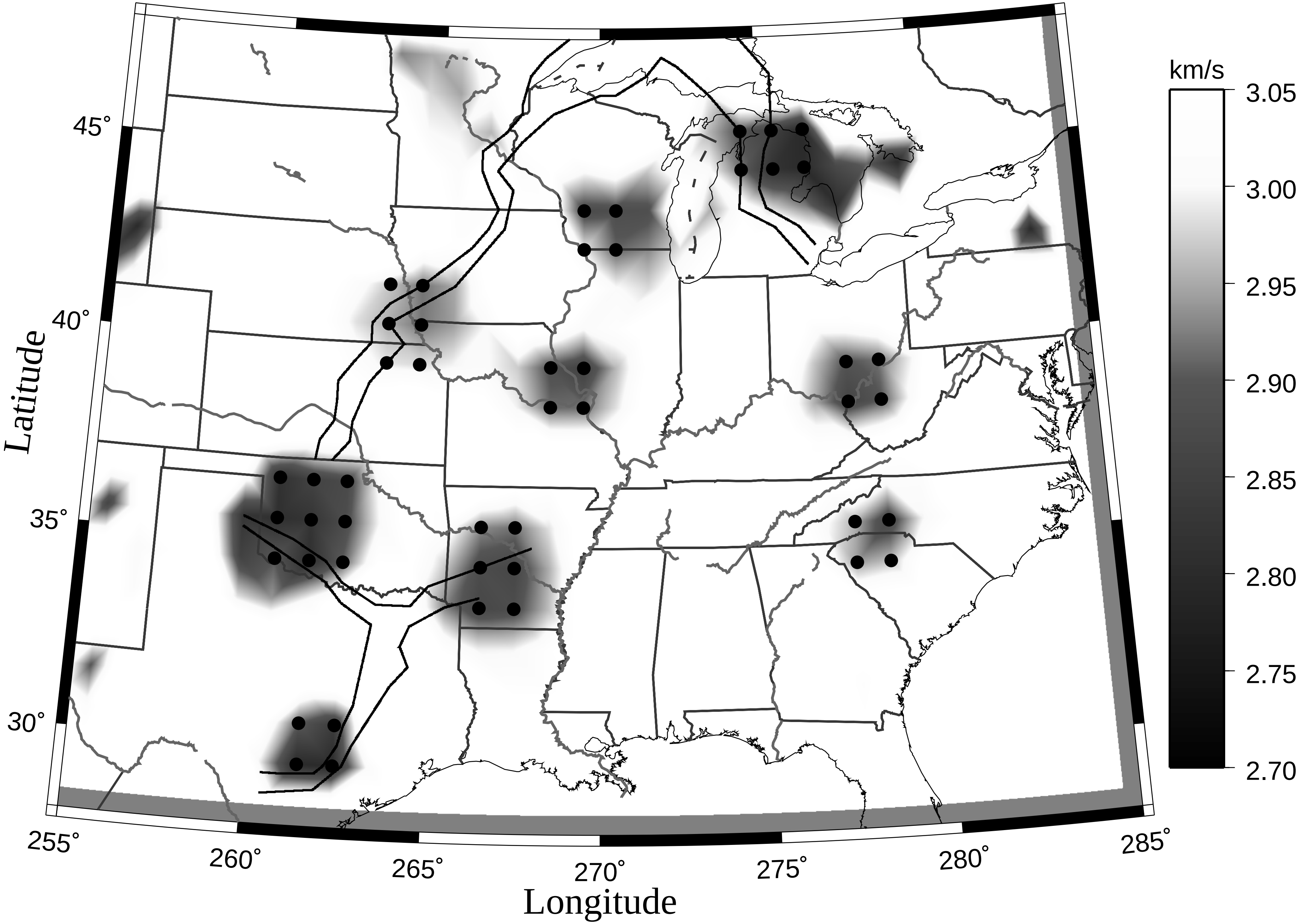
km/s
3.05
3.00
2.95
2.90
2.85
2.80
2.75
2.70
45°
40°
35°
30°
Latitude
255°
260°
265°
270°
275°
280°
285°
Longitude